

The Leo Elliptical NGC 3379: A Metal-Poor Halo Emerges¹

William E. Harris

Department of Physics & Astronomy, McMaster University, Hamilton L8S 4M1, Canada

`harris@physics.mcmaster.ca`

Gretchen L. H. Harris

Department of Physics & Astronomy, University of Waterloo, Waterloo N2L 3G1, Canada

`glharris@astro.uwaterloo.ca`

Andrew C. Layden

Department of Physics and Astronomy, Bowling Green State University, 104 Overman Hall, Bowling Green, OH 43403

`layden@baade.bgsu.edu`

Elizabeth M. H. Wehner

Department of Physics & Astronomy, McMaster University, Hamilton L8S 4M1, Canada

`wehnere@physics.mcmaster.ca`

ABSTRACT

We have used the ACS camera on HST to obtain (V, I) photometry for 5300 red-giant stars in the halo of the dominant Leo-group member NGC 3379, a galaxy usually regarded as a classic normal giant elliptical. We use this sample of stars to derive the metallicity distribution function (MDF) for its outer-halo field stars at a location centered 33 kpc from the galaxy center. In at least two ways the MDF is distinctly unlike all the other E galaxies for which we have similar data (including the Local Group dwarf ellipticals, the intermediate-luminosity NGC 3377, and the giant NGC 5128). First, the MDF for the NGC 3379 outer halo is extremely broad and flat, with many stars at every interval in $[m/H]$ and only a gradual rise towards higher metallicity. Second, we see a metallicity gradient across our ACS field such that in its outermost region the blue, low-metallicity stars ($[m/H] < -0.7$) are beginning to dominate and the higher-metallicity stars are rapidly diminishing. In order to successfully match this extremely broad

MDF, we find that a distinct two-stage chemical evolution model is necessary. Our target field is centered at a projected distance about equal to $12R_e$, twice as far out in units of effective radius as in any of the other galaxies that we have surveyed. If NGC 3379 is indeed representative of large E/S0 galaxies, we predict that such galaxies in general will reveal diffuse low-metallicity subpopulations, but that photometry at radii $r \simeq 10 - 15R_e$ will be necessary to get beyond the edge of the dominant metal-rich component and to see the faint low-metallicity component clearly. Finally, we discuss possible connections of these outer-halo stars with the metallicity distributions that are beginning to be observed in the intracluster medium of nearby rich galaxy clusters, which also show flat MDFs. These outermost-halo observations are challenging, but ones which may give an unusually direct window into the earliest star-forming stages of these galaxies.

Subject headings: galaxies: elliptical— galaxies: individual (NGC 3379)

1. Introduction

The imaging tools provided by the Hubble Space Telescope have revolutionized our ability to study the stellar populations in nearby galaxies, at depths and resolutions that have been impossible with ground-based instruments. Particularly for the oldest stellar populations – the halo stars, bulge stars, and globular clusters – these deep and precise HST-based photometric studies have opened a major route to understanding the early chemical evolution of their host galaxies that was previously available only for the Local Group members.

The giant elliptical galaxies attract special interest because they may result from the widest possible range of formation histories, all the way from hierarchical merging at very early times, to recent major mergers, to later growth by satellite accretion. When considered along with the dwarf ellipticals within the Local Group (NGC 147, 185, 205, M32, and the many dwarf spheroidals), we can, at least in principle, piece together the evolutionary histories of E galaxies over their full mass range.

¹Based on observations made with the NASA/ESA Hubble Space Telescope, obtained at the Space Telescope Science Institute, which is operated by the Association of Universities for Research in Astronomy, Inc., under NASA contract NAS 5-26555. These observations are associated with program #9811. Support for this work was provided in part by NASA through grant number HST-GO-09811.01-A from the Space Telescope Science Institute, which is operated by the Association of Universities for Research in Astronomy, Inc., under NASA contract NAS 5-26555.

The nearest giant E/S0 galaxy is NGC 5128, the dominant member of the Centaurus group at $d = 3.8$ Mpc. In a series of previous papers (Harris, Harris, & Poole 1999; Harris & Harris 2000, 2002; Rejkuba et al. 2005), we have discussed photometric analyses of its halo and bulge stars covering field locations at projected distances ranging from 8 to 40 kpc. In all four of these studies the red-giant branch (RGB) stars are clearly resolved, and in the deepest one (Rejkuba et al. 2005), even the old horizontal-branch population is reached. Intriguingly, throughout every part of its halo that we have surveyed so far, the *metallicity distribution function* (MDF) of the giant stars is clearly metal-rich (with a mode near $[\text{Fe}/\text{H}] \simeq -0.4$) and with extremely small proportions of classically metal-poor stars in the range $[\text{Fe}/\text{H}] < -1$. However, uncertainties continually surround any attempt to generalize NGC 5128 to all large ellipticals because of its evident history of satellite accretion from within the Centaurus group (e.g. Israel 1998; Peng et al. 2002; Woodley 2006; Malin et al. 1983; Tubbs 1980; Quillen et al. 1993). The possibility of a larger merger has been modelled by Bekki & Peng (2006). In addition, models show that both a major-merger and a hierarchical-merging approach are capable of creating an MDF with the same basic characteristic of a predominantly metal-rich halo (Bekki & Chiba 2001; Bekki et al. 2003; Beasley et al. 2003), although the mechanisms in each case are different: in a major merger, the halo ends up being populated by the metal-rich stars in the disks of the colliding progenitors; while in hierarchical merging, the metal-rich stars accumulate in the long series of small and large starbursts that construct the galaxy as a whole. Even though many large ellipticals share the same kinds of features with NGC 5128, it is necessary to extend these studies to other targets to gain the complete picture that we need.

The next nearest readily accessible E galaxies are in the Leo group at $d \sim 10$ Mpc, including the intermediate-luminosity NGC 3377 and the giant NGC 3379. The E1 giant NGC 3379 (Messier 105) is an especially attractive target because it is, quite literally, a textbook giant elliptical (e.g. Carroll & Ostlie 2007). It is a keystone (de Vaucouleurs & Capaccioli 1979) in establishing the classic de Vaucouleurs photometric profile; Statler & Smecker-Hane (1999) refer to it engagingly as “virtually a walking advertisement for the $r^{1/4}$ law”. With a luminosity $M_V^T = -20.85$, a smooth and nearly round profile shape, no strong photometric peculiarities, and a nearby location in a high-latitude field, it has for decades been regarded as a baseline “normal” elliptical.² A detailed study of its halo stars is within reach of the HST ACS camera, and thus holds out considerable promise for giving us new insight into the stellar populations of classic giant ellipticals. Table 1 summarizes its basic parameters.

²A more generally flexible model for matching a wider range of E galaxy profiles is the generalized Sersic model (e.g. Ferrarese et al. 2006) or core-Sersic model with index n depending on luminosity; the traditional de Vaucouleurs profile is a special case of this family.

NGC 3379 fits well into the E-galaxy sequence in other ways. Its central black hole mass of $M_{BH} \simeq 1.4 \times 10^8 M_\odot$ (Shapiro et al. 2006) closely follows the normal $M_{BH} - \sigma$ relation. Its velocity field and dynamical structure are well behaved out to $R_{gc} \sim 90'' \simeq 2R_e$ (Shapiro et al. 2006) and large-scale surface photometry shows no shells or other remnants of mergers or accretions (Schweizer & Seitzer 1992) and very little gas (see Statler & Smecker-Hane 1999, for a review). The possibility has been discussed that it may actually be an S0 or modestly triaxial configuration seen nearly face-on, since the right combinations of disk, bulge, and inclination angle could mimic a global $r^{1/4}$ profile (Statler & Smecker-Hane 1999; Capaccioli et al. 1991; Shapiro et al. 2006). The velocity field within $R < R_e$ may also be more consistent with an S0 structure (Statler & Smecker-Hane 1999). In the discussion below, other evidence will be mentioned that may also be consistent with an S0 classification.

Previous studies of the resolved old red giant stellar populations in NGC 3379 have been published by Sakai et al. (1997) and Gregg et al. (2004). Sakai et al. (1997) used HST WFPC2 exposures in a field $6'$ west of galaxy center in a single filter (the $F814W$ “wide I ” band) in order to calibrate the distance from the tip of the red-giant branch. Gregg et al. (2004) used HST *NICMOS* J and H exposures in three fields, one of them located within the Sakai WFPC2 field and the other two further in, at $R_{gc} = 3'$ and $4.5'$ from galaxy center. They found that the mean metallicity for the RGB stars in these fields was near Solar abundance, but since metal-poor stars are significantly fainter than metal-rich ones in the near infrared, they left open the possibility that the mean $[m/H]$ might be overestimated. At fainter levels in their color-magnitude diagrams, low-metallicity stars with $[m/H] < -1$ may begin to appear, but the larger photometric measurement scatter there leaves uncertainties about the relative numbers versus metallicity. At the opposite end of the abundance scale, stars of metallicity $[m/H] = +0.4$ and even higher could also be present according to the range of colors they observe in the CMD. Direct comparison of similar *NICMOS* photometry for an inner-halo field in NGC 5128 by Marleau et al. (2000) indicates that the *mean* stellar metallicities are both near Solar in these two galaxies but that the internal metallicity spread in NGC 3379 is higher. We emphasize, however, that both of these studies have targeted the inner halos of these gE galaxies and thus must be sampling predominantly the bulge (or disk) population that is expected to be metal-rich.

In this paper, we present new color-magnitude photometry for the halo stars in NGC 3379. The observations and analysis techniques are the same as in our companion study of the other Leo elliptical, NGC 3377 (Harris et al. 2007). Although we expected to find that the NGC 3379 halo would be metal-rich following the pattern established by the other ellipticals already studied, the results have turned out differently.

2. Observations and Data Reduction

Our imaging data for both NGC 3377 and 3379 were obtained in HST program 9811. We used the Advanced Camera for Surveys in its Wide Field Channel, which has an image scale $0''.05$ per pixel. Our NGC 3379 target field was centered at $\alpha = 10^h47^m06^s.5$, $\delta = +12^\circ37'46''.9$ (J2000). This field is $630''$ west and $173''$ north of the center of NGC 3379, equivalent to $R_{gc} = 10'.9 \simeq 33$ kpc projected radius at our adopted distance of 10.2 Mpc (see below for the distance calibration). The galaxy light profile has an effective radius $R_e = 0'.93 \simeq 2.8$ kpc, putting our target field at $R_{gc} \simeq 11.7R_e$. We deliberately selected a location about twice as far out as the WFPC2 field location used by Sakai et al. (1997) to avoid any concerns about image crowding, as well as to ensure that we would be gathering a sample of stars that could be viewed as a genuine “halo” population different from the inner fields in these previous studies. The field placement is shown in Figures 1 and 2.

The comprehensive surface-photometry studies of de Vaucouleurs & Capaccioli (1979) and Capaccioli et al. (1990) found that NGC 3379 has isophotal contours with a mean ellipticity $\langle b/a \rangle = 0.88$ and a major axis orientation 70° E of N (or 110° W of N). Our target field, relative to the galaxy center, lies in a direction 75° W of N and thus is at an angle of 35° off the major axis. On the opposite (east) side of NGC 3379 is the disk galaxy NGC 3384, at $\alpha = 10^h48^m16^s.9$, $\delta = +12^\circ37'46''$. Our ACS field is thus nearly due west of NGC 3384 and $1030''$ away. Since NGC 3384 is nearly twice as far away as NGC 3379, and only about half as luminous, we expect the stellar population visible on our target field to be completely dominated by the giant elliptical.

We used the ACS/WFC “wide V” ($F606W$) and “wide I” ($F814W$) filters, the same ones as in our previous studies of NGC 5128 (Harris, Harris, & Poole 1999; Harris & Harris 2000, 2002; Rejkuba et al. 2005) and NGC 3377 (Harris et al. 2007). As we discuss in those papers, the $(V - I)$ color index is an effective metallicity indicator for old red giant stars over the full metallicity range from $[\text{Fe}/\text{H}] \sim -2$ up to Solar abundance, and particularly for $[\text{Fe}/\text{H}] \gtrsim -1.5$. Over this full metallicity range, the corresponding spread of $(V - I)$ colors is more than 2 magnitudes at the top of the giant branch (see the color-magnitude diagrams plotted below), a range more than twice as large as the ~ 0.8 -mag color spread in near-infrared indices such as $(J - H)$ (Gregg et al. 2004). The second major advantage that optical color indices have over infrared ones is the very much bigger detector area, so that that statistically larger sample sizes can be accumulated much faster.

In the $F606W$ filter our total exposure time was 38500 sec split over 15 exposures; for $F814W$, the total was 22260 sec over 9 exposures. In the original series of exposures, half the $F606W$ images were ruined by camera shutter and readout failure; fortunately, these were repeated successfully a year later. Recovering the full series of images proved to be

crucially important to our main goal of interpreting the metallicity distribution function of the halo stars, because our detection of the reddest (thus most metal-rich) RGB stars is set by the photometric limits in the V filter. The final exposures were identical with the totals for our NGC 3377 data, although (as will be seen below) the NGC 3379 data reach slightly deeper because of decreased effects of crowding. The individual exposures in the series were dithered over several step sizes up to 20 pixels, allowing elimination of most cosmic rays, bad pixels, and other artifacts on the detector. To prepare the images for photometry, we extracted the drizzled individual images from the HST Data Archive, registered them to within 0.05 pixels, and median-combined them. This procedure gave us a single very deep exposure in each filter. In Figure 2, we show the combined I -band image.

Our procedures for object detection and photometry were identical with those for NGC 3377 (Harris et al. 2007) and are more fully described there. In summary, we used the standalone version of *DAOPHOT* codes in its fourth-generation *daophot 4* version, with the normal sequence of *find/phot/allstar*. The primary difference during the *daophot* stage compared with our companion NGC 3377 study was that the number density of stars was about one full order of magnitude lower than on our NGC 3377 field, so that we had to select candidate bright, isolated stars to define the point spread function by visual inspection to weed out the many similarly bright but nonstellar background galaxies. In the end, the PSF was defined from an average of 15 to 20 stars on each frame. The FWHM of the point spread function is 2.3 px or $0''.115$.

The detected objects on each of the two master images were matched up to isolate those measured in both colors. At this stage, any objects with *allstar* goodness-of-fit parameters $\chi_V > 1.5$ or $\chi_I > 1.2$ were rejected, leaving a total of 5642 matches. Not all of these, however, are stars. The biggest single issue we had to deal with in this dataset was not crowding or faintness; in absolute terms this outer-halo field is completely uncrowded, and the brightest red giants in the galaxy are quite well resolved. Instead, the main problem was *field contamination* by faint background galaxies, which appeared in larger numbers on this particular region of sky and made up a relatively much higher proportion of the total population of objects on the frame than in our NGC 3377 field. To define the cleanest possible subset of data, first we masked out circles around more than a hundred of the biggest field galaxies in the field, which are “detected” by *daophot/find* as multiple closely spaced clusters of PSFs, all of which are invalid. This step eliminated 10 percent of the total field area. Next, we ran the SExtractor object detection and classification code (Bertin & Arnouts 1996) and rejected any objects with “stellarity” index less than 0.3 (although many of these had in fact already been rejected in the *daophot/find* and *allstar* steps). Finally, we used extremely careful visual inspection of all the remaining objects brighter than $I \simeq 27.5$ (which is about 1.5 mag below the red-giant-branch tip; see below) to pick out any other definitely

nonstellar or closely crowded objects. This series of steps left us with a final total of 5323 stars. For comparison, we obtained a total of 57039 stars in NGC 3377 over the same ACS field area, where the pointing was relatively closer to the galaxy center.

Calibration of the photometry followed exactly the same steps described in Harris et al. (2007). The adopted transformations between the $F606W$ and $F814W$ magnitudes on the natural ACS VEGAMAG filter system, and the standard V and I , are repeated here for convenience:

$$F606W = V - 0.265(V - I) + 0.025(V - I)^2 \quad (1)$$

$$F814W = I + 0.028(V - I) - 0.008(V - I)^2 \quad (2)$$

We next carried out conventional artificial-star tests to determine the internal photometric uncertainties and the detection completeness. Scaled PSFs were added to the master images 1000 at a time over a wide range of magnitudes, independently on the $F606W$ and $F814W$ images, and the images were then remeasured in exactly the same way as the original frames. A total of 10,000 fake stars were used in V and 8000 in I . For relatively uncrowded frames such as these, the fraction f of stars recovered, as a function of instrumental magnitude, is well described by a Pritchett interpolation curve (Fleming et al. 1995),

$$f = \frac{1}{2} \left[1 - \frac{\alpha(m - m_0)}{\sqrt{1 + \alpha^2(m - m_0)^2}} \right] \quad (3)$$

which has two free parameters: the limiting magnitude m_0 where $f = 0.5$, and the slope α giving the steepness of the f -dropoff through the m_0 point. For our data we find $m_0(F606W) = 29.20$ and $m_0(F814W) = 28.10$, along with $\alpha(F606W) = 2.8$, $\alpha(F814W) = 3.0$. These limits are both $0.25 - 0.3$ mag deeper than in our NGC 3377 field.

The artificial-star tests can also be used to estimate the internal random uncertainties of the photometry, as well as any systematic bias in the measured magnitudes as functions of magnitude. No biases larger than 0.03 mag in either filter were found for stars brighter than the completeness limit m_0 , and the resulting biases in the color indices ($V - I$ or $F606W - F814W$) are completely negligible. The mean random uncertainties are represented accurately by gradually increasing exponential interpolation curves,

$$\sigma(F606W) = 0.01 + 0.03 \exp((F606W - 27.0)/1.09) \quad (4)$$

$$\sigma(F814W) = 0.01 + 0.03 \exp((F814W - 26.0)/1.15). \quad (5)$$

Over our primary magnitude range of interest ($I \lesssim 27$) the measurement uncertainties are less than ± 0.1 mag, much less than the intrinsic spread in colors for the bright RGB stars we

are studying. Although these interpolation equations indicated that the *internal* precision of the photometry is only $\simeq 0.01$ mag at the bright end, the true (external) uncertainty could be $\pm 0.02 - 0.3$ mag because of other factors such as systematic variations of the PSF across the field and accuracy of flat-fielding. However, photometric uncertainties at any such level are trivial compared with the > 1 -mag range in $(V - I)$ colors that we use for metallicity determination.

An important feature of the completeness limits is that the limiting curve for V cuts off our ability to see any extremely red stars that might actually be present; these would fall at the most metal-rich end of our metallicity distribution function. Considerably deeper exposures in V will be needed to explore the true “red limit” of the giant stars in this galaxy. Within the limits imposed by the photometry, we explicitly take into account the completeness fraction f in our derivation (below) of the metallicity distribution. Near-infrared photometry would be sensitive to this high-end range of metallicities (Gregg et al. 2004), but as noted earlier, the accompanying huge penalty is the smaller area of the infrared detectors and loss of statistical weight in sample size.

3. The Color-Magnitude Diagram

The color-magnitude diagram (CMD) of our final sample of 5323 stars is shown in Figure 3. The presence of a substantial *blue* RGB population in the color range $1 \lesssim (V - I) \lesssim 1.6$ is immediately evident, along with many redder RGB stars that continue redward till the $F606W$ completeness cutoff line (dashed line at right). The first impression is therefore that the halo has primarily a *blue, metal-poor* giant branch like those in dwarf ellipticals (e.g. Han et al. 1997; Butler & Martinez-Delgado 2005). However, this initial reaction about the relative numbers of stars at various metallicities is deceptive because of the strongly nonlinear dependence of color on metallicity, as will be discussed in Section 5 below.

The region to the blue side of the RGB (those with $(V - I) < 0.9$ and $I > 27$) also has some objects scattered across it, and is more well populated than in our NGC 3377 data. If real, it might suggest the presence of a young population. However, the great majority of these blue objects appear, once again, to be due simply to field contamination. A plot of the xy positions of these very blue objects shows that they are rather uniformly scattered over the field, as would be expected for a background or foreground population (see the discussion in Section 8 below for an analysis of spatial gradients in the RGB stars), although a shallow gradient would be hard to detect with this small number of stars. A more incisive test is from direct examination of our images, which suggests that most of the very blue objects are noticeably nonstellar, or crowded, or both. However, for objects this faint it

is extremely difficult for objective routines such as *daophot* or SExtractor, or even careful eye inspection, to classify and separate them cleanly from stars. In this range as well, the photometric measurement errors become large enough to contribute a noticeable spread in the RGB color distribution, as is evident in the CMD.

Pursuing the tests for a younger population a bit further, we have experimented with the placement of isochrones of various ages on the CMD. If these blue objects are young, moderately metal-rich stars, they would have to be near 10^8 yr and older to pass through the relevant region of the CMD. A population of such stars should also produce an AGB branch extending up above the RGB tip, which does not appear (cf. Williams et al. 2007, for examples of this type of feature). In addition, star formation within the past 10^8 yr could also be expected to leave residual gas, for which little evidence exists. In sum, it seems appropriate to conclude that most of these objects are simply field contamination.

The classification steps that we carried out (see above) are much more definitive for $I < 27$, which fortunately is the range that we rely on for our results (the MDF and the distance measurement). In this key upper RGB range, we are working with a sample of well defined, isolated stars. Over the color range $(V - I) \gtrsim 1.0$, the stars can easily be interpreted as the halo RGB population over a range of metallicities.

The last region of the CMD calling for particular comment is the section brighter than the RGB tip (TRGB). We have already noted that no obvious younger AGB-like branch is present in this supra-TRGB area, and of the $\simeq 40$ stars lying clearly above the TRGB, half of them can be understood simply as foreground field-star contamination (we expect $\simeq 20$ from Galactic starcount models; e.g. Bahcall & Soneira 1981). The normal, old RGB can also produce some brighter objects, such as LPVs in temporary luminous stages (Renzini 1998; Harris et al. 2007), and accidental blends of RGB stars that are measured as brighter singles. LPVs and similar objects are present in proportion to the total RGB population, while the number of accidental blends due to crowding goes up as N_\star^2 . For our similar studies of NGC 3377 (Harris et al. 2007) and the bulge region of NGC 5128 (Harris & Harris 2002), the numbers of stars above the RGB tip were significantly larger, driven by the much higher density of stars. For this very uncrowded NGC 3379 field, we expect $\simeq 10 - 20$ LPVs but essentially no accidental blends. In summary, the total of all expected sources of supra-RGB sources matches the number we see to within statistical uncertainty.

As a final approximate but more direct test for the presence of LPVs, we used the fact that the *F606W* images were taken in two groups at widely separated epochs to search directly for bright variables. We median-combined the first six *F606W* exposures taken in 2004 to make a single, cleaned image, and similarly combined the four additional *F606W* exposures taken almost exactly one year later to make a second cleaned image. We then

ran the normal sequence of *find/phot/allstar* on these two images as described in Section 2 and merged the photometry files using *daoamaster*. Only stars that were retained in the culling steps described in Section 2 were considered. Stars showing a magnitude difference ΔV between the two epochs (including stars found in one but not the other epoch) greater than seven times their measurement uncertainties were considered candidate variables. We inspected these stars on the two images to verify that the magnitude variations were not affected by incomplete filtering of cosmic rays or other image artifacts. This procedure gave us a list of eight LPV candidates. We also visually inspected all stars with $I < 26$ and $V - I > 3$ mag, since these red, metal-rich stars are also good candidates for LPVs. The three brightest such stars appear distinctly in one image but not the other, so are likely to be LPVs as well. While several of the total of 11 LPV candidates have magnitude differences $\Delta V > 1.0$ mag, others are closer to the limit of detection. Given that we have sampled the data at only two distinct epochs as well, we therefore expect there are other LPVs in the field that we were unable to detect. The 11 LPV candidates are marked in the CMD of Fig. 3.

In summary, the number of candidate LPVs that we have identified is consistent with our rough estimates above that were based only on the population statistics of the RGB. These 11 LPVs, together with the $\simeq 20$ field stars, already account for most or all of the subra-RGB sources seen in Fig. 3, to within statistical uncertainty.

4. Distance Calibration

Most of the large galaxies in the Leo I group are disk systems, while NGC 3379 is the largest elliptical. In Harris et al. (2007), we summarize the previous measurements of distance to individual Leo members from a variety of well established distance indicators including Cepheids, planetary nebula luminosity function (PNLF), surface brightness fluctuation (SBF), and the tip of the old red-giant branch (TRGB). The overall average for 5 large galaxies including both NGC 3377 and NGC 3379 (see Harris et al. 2007) is $\mu = (m - M)_0 = 30.1 \pm 0.05$, or $d = 10.4$ Mpc. The galaxy-to-galaxy dispersion of these measurements ($\sigma_\mu = 0.17$ mag) is comparable with the internal uncertainties of each method.

For NGC 3379 specifically, the TRGB method as applied through WFPC2 photometry in the optical I band (Sakai et al. 1997) gave $\mu = 30.30 \pm 0.27$, while the same method from HST/NICMOS in the near infrared (Gregg et al. 2004) gave $\mu = 30.17 \pm 0.12$. The PNLf method (Ciardullo et al. 1989) yielded $\mu = 29.96 \pm 0.16$, and the SBF method (Tonry et al. 2001) $\mu = 30.12$.

Our new ACS photometry penetrates well into the old-halo red giant branch with a cleanly defined sample, and provides a new opportunity to use the TRGB distance indicator more precisely than before. The brightest detectable RGB stars, by hypothesis, define the “tip magnitude” or TRGB, which represents the luminosity of the helium flash at the end of the stars’ first ascent along the giant branch. Empirically, we plot the luminosity function of the RGB stars in the I band and use the sharp rise in the LF to define the onset of the RGB. The method is outlined by Sakai et al. (1996, 1997) and Harris, Harris, & Poole (1999) and these papers can be seen for further discussion of the technique. For stars more metal-poor than $[\text{Fe}/\text{H}] \simeq -0.7$ (which include the majority of the ones we measure here; see next section), the I band has the strong advantage that the differential bolometric correction across the top of the RGB is almost cancelled by the opposite dependence of $M_{\text{bol}}(\text{tip})$ on metallicity, leaving only a gradual decrease of $M_I(\text{tip})$ with increasing color.

We show the luminosity function in Figure 4. The version shown here has been smoothed with a Gaussian kernel of $\sigma_I = 0.02$ mag, although the result is insensitive to the particular smoothing width. Completeness corrections are also quite unimportant here, since the $f = 0.5$ completeness level is considerably fainter than the well resolved top of the RGB. In essence, we look for the maximum change in the LF slope near that point by using the numerically calculated first and second derivatives of the LF (shown in the lower two panels of Fig. 4 and referred to as the “edge response filter” or ERF). These show that the first sharp peak is at $I = 26.10 \pm 0.10$, which we adopt as the TRGB.

The distance modulus follows immediately once we apply a fiducial value for $M_I(\text{tip})$. As we did in our NGC 3377 study, we adopt $M_I(\text{tip}) = -4.05 \pm 0.12$ from the comprehensive photometric study of ω Cen by Bellazzini et al. (2004), which is entirely consistent with the range given by recent theoretical RGB models (e.g. Salaris et al. 2002) depending on the details of the input stellar physics. We therefore obtain $(m - M)_I = 30.15 \pm 0.15$ for NGC 3379. This must be corrected for the foreground absorption of $A_I = 0.05 \pm 0.02$, giving a final TRGB distance measurement $\mu = 30.10 \pm 0.16$. This result is entirely consistent with the previous TRGB measurements (Sakai et al. 1997; Gregg et al. 2004) within their internal uncertainties.

Averaging our TRGB distance in with the SBF and PNLf measurements listed above, and giving the three methods equal weights, we arrive at an average $(m - M)_0 = 30.06 \pm 0.10$, or $D = 10.2 \pm 0.5$ Mpc for NGC 3379. These three methods give a result which puts NGC 3379 near the average for the Leo group as a whole, and is consistent with it being close to the dynamical center of the group. By comparison, our result for the smaller elliptical NGC 3377 from exactly the same method placed it 0.10 mag more distant than NGC 3379. This differential distance is just on the margin of being significant relative to the internal

uncertainty of the TRGB method and suggests that the Leo group may have a minimum line-of-sight “depth” of ~ 1 Mpc.

5. The Metallicity Distribution

With the CMD and the distance calibration in hand, we are in a position to derive the metallicity distribution function for the halo of this galaxy. To facilitate the most direct possible comparisons with other systems, we follow precisely the same method as in our previous studies (Harris & Harris 2002; Rejkuba et al. 2005; Harris et al. 2007). We place a finely spaced grid of RGB evolutionary tracks for 12-Gyr-old stars (the α -enhanced tracks of VandenBerg et al. 2000) on the measured CMD, suitably registered to match the observed RGB sequences for Milky Way globular clusters. Interpolation within the fiducial tracks is then carried out to estimate the heavy-element abundance Z of each RGB star. The details of this technique are described fully in Harris & Harris (2002) and we do not repeat them here. However, as before, we strongly emphasize that the metallicity scale is an *observationally calibrated one* based on real globular clusters. *The theoretical models are used only to aid interpolation between the observed sequences for real clusters.*

We use the 12-Gyr models as a plausible age estimate for old halo stars and globular clusters, while also realizing that for low-mass stars older than ~ 5 Gyr the $(V - I)$ colors are only very weakly sensitive to age (e.g. Harris, Harris, & Poole 1999; Rejkuba et al. 2005). If the stars in our target galaxy are actually younger than 12 Gyr, then this method would slightly underestimate their Z -abundances since the RGB locus shifts blueward at lower age. But because the shift is only at the rate of $\Delta \log Z \sim 0.1$ dex per 4-Gyr age difference, the metallicity spread is by far the dominant effect in driving the large color range that we see across the top of the RGB.

In Figure 5 we show the CMD with the RGB tracks added. The two tracks shown as dashed lines at right are ones for Solar ($Z = Z_{\odot}$) and $\simeq 3Z_{\odot}$ metallicities; both of these fall past the 50% photometric completeness level in V and thus imply that *if* this remote outer part of the NGC 3379 halo does contain any such stars, most would not be detectable in our data. Considerably deeper exposures in V will be needed to find them unambiguously.

The derived MDF, plotted in conventional form as number of stars per unit $[\text{m}/\text{H}] = \log(Z/Z_{\odot})$, is shown in Figure 6, where we divide the sample into half-magnitude bins by approximate luminosity M_{bol} . Fig. 6 explicitly shows the MDF with, and without, photometric completeness corrections. Any stars fainter than the $f = 50\%$ line in *either* $F606W$ or $F814W$ have been rejected from the sample, since at these levels the completeness correction

itself becomes dangerously large and the random and systematic errors of the photometry increase rapidly. For all stars brighter than the 50% cutoff, the completeness-corrected samples (the open histograms in Fig. 6) have been constructed by weighting each star individually as $(1/f)$ where $f = f_I \cdot f_V$ is the combined completeness fraction at its particular location in the CMD. For comparison, the unweighted MDF (based only on counting up all stars with $f > 0.5$) is shown in the hatched regions. The completeness corrections affect the shape of the MDF histogram in an important way only for $[m/H] > -0.3$.

The faintest of the three bins reaches into the $I > 27$ magnitude range that is still likely to be affected to some extent by field contamination (see the preceding discussion), but any such contamination does not seem to have skewed the overall shape of the MDF by comparison with the two brighter bins. Nevertheless, in the following discussion we use only the brightest ($M_{bol} < -2.5$) part of the data, corresponding roughly to the uppermost magnitude of the RGB.

The shape of the MDF is a surprise. The previous results from other E galaxies including NGC 3377 (Harris et al. 2007), NGC 5128 (Harris & Harris 2002), and also M32, a galaxy near the lower limit of the normal E sequence (Grillmair et al. 1996), as well as the near-infrared NGC 3379 data of Gregg et al. (2004), appeared to establish a pattern in which a large spread of RGB metallicities is present but where the great majority of stars are metal-rich with MDF peaks in the range $\langle m/H \rangle \simeq -0.7$ to -0.3 depending on galaxy luminosity. However, both the distribution of the stars on the NGC 3379 CMD, and its transformed version in Fig.6, are strikingly unlike any of the other systems. The MDF is the broadest and flattest one we have ever seen. Once the transformation from $(V - I)$ to $[m/H]$ has been made, we find that this part of the halo is not dominated by either low-metallicity or high-metallicity components. The mode of the distribution seems to be near $[m/H] \sim -0.5$, but unlike all the other galaxies cited above, there is really no interval in the MDF that is genuinely dominant. Neither can the MDF shape be described easily as “bimodal” as is the case for almost all globular cluster systems in large galaxies, where roughly equal numbers of clusters concentrate near $[m/H] \simeq -1.5$ and $\simeq -0.5$ (e.g. Peng et al. 2006; Harris et al. 2006). In addition, since the MDF is still not declining very rapidly at the upper end where it hits the photometric completeness cutoff, it seems likely that it actually continues up to and beyond Solar metallicity (Gregg et al. 2004) and that we are seeing only a lower limit to its full extent. In the discussion below, we will estimate more quantitatively how many more metal-rich stars we are likely to be missing from the complete MDF.

6. Matching to Chemical Evolution Models

To gain a bit more insight into the possible formation history of NGC 3379, we next try to step beyond the raw MDF into a chemical evolution model.

In our series of studies of NGC 5128 we developed a simple, semi-analytic chemical evolution model that has been applied successfully to all the NGC 5128 fields, to NGC 3377 (Harris et al. 2007), and to the dwarf ellipticals (Harris, Harris, & Poole 1999; Butler & Martinez-Delgado 2005). Very similar models have also been used for the halo of the Milky Way (Prantzos 2003), and the globular cluster systems of large galaxies (Vandalfsen & Harris 2004), among other situations. Briefly, in this first-order model we envisage an “accreting box” in which a region of initial gas mass M_0 turns itself into stars through a long succession of star-forming episodes, during which more gas is continuously flowing into the region. Although in reality this star-forming sequence will happen continuously, for numerical calculation purposes we suppose it to happen in a series of small discrete timesteps δt . By hypothesis, the rate of gas infall is allowed to die away with time, so that in the late stages of the region’s history, its chemical evolution asymptotically approaches the classic “closed-box” or “Simple” model (Pagel & Patchett 1975). By carrying out a straightforward numerical integration, we then compute the total number of stars at a given metallicity (that is, the model MDF) once all the gas has been used up. As we discuss in the papers cited above, this model is an approximate description of what would be expected to happen during hierarchical merging of a large set of initial, zero-metallicity gas clouds within which star formation is taking place simultaneously as they merge to form a bigger final galaxy.

In Harris & Harris (2002) we outline and justify the key assumptions in the model:

- The gas infall rate starts at a chosen level and then dies away as an exponential decay with time.
- At each star formation step δt , the same fraction of ambient gas gets turned into stars (we adopt a 5% conversion rate for purposes of the numerical calculations).
- Each timestep assumes “prompt mixing”, i.e. at each stage the remaining gas in the region has a uniform $Z(gas)$.
- The abundance Z of the stars forming at any given moment then equals the abundance of the gas left behind by the previous steps, mixed with the new gas entering the region just before the next star formation step occurs.
- The “effective yield” y_{eff} of the stellar nucleosynthesis (the fraction of stellar mass that is expelled back into the interstellar medium as enriched heavy elements) is assumed

to stay constant throughout the sequence.

The model has a minimum of three free parameters: (1) the effective yield y_{eff} , which combines the effects of both the true nucleosynthetic yield y and any SN-driven outflow that drives gas out of the system (cf. Binney & Merrifield 1998); (2) the initial gas infall rate $(\dot{M}/M)_0$ relative to the amount of gas initially present in the region; and (3) the exponential decay time τ_2 for the infall rate. Other potentially useful parameters include (4) an initial time period τ_1 over which the infall rate \dot{M} stays roughly constant; and (5) the heavy-element abundance Z_{in} of the added gas. The so-called closed-box or Simple Model is a special case where we set \dot{M}, τ_1, τ_2 equal to zero, leaving only y_{eff} as the single free parameter.

An extremely instructive way to study the match between model and data is through the linear form of the MDF, which is the number of stars per unit heavy-element abundance Z/Z_\odot . In this graph, the closed-box model would look simply like an exponential decline in dn/dZ , the number of stars per unit heavy-element abundance. In Figure 7, we replot the Z -histogram of our data along with two particular cases of a closed-box model. The models shown in Fig. 7 can match either the high- Z or low- Z end of the data, but no single choice of y_{eff} fits the entire run, so the Simple model is not even approximately valid.

For NGC 5128, NGC 3377, and the dwarf ellipticals, we found that although a closed-box evolution does not fit them either, it is possible in each case to start from primordial material $Z_{in} = 0$ and then to find an accreting-box solution with reasonable choices of y_{eff} , τ_2 , and \dot{M}_0 that gives an excellent match to the data. NGC 3379 is unlike all these previous cases. Experimentation with the accreting-box model shows that *no single chemical evolution sequence of this type* can fit this MDF.

The next step is to try a multi-stage model. We show one such solution in Figure 8 which provides reasonable success, and which assumes that the formation process happened in two rather distinct stages. The parameters for each stage are:

- *Metal-poor component:* A closed-box model with $\dot{M} = 0$, $y_{eff} = 0.1Z_\odot$, and a truncation of the timestep sequence near $Z = 0.2Z_\odot$. This truncation point is adopted as the obvious point above which the simple model with low yield $y_{eff} = 0.1Z_\odot$ can no longer match the data (see Figure 7). We use a sharp truncation only for numerical simplicity; a steep but smoother ramp-down at that point would work equally well.
- *Metal-rich component:* An accreting-box model with $Z_{in} = Z_0 = 0.19Z_\odot$ (that is, both the initial abundance and the infalling gas have the same, nonzero enrichment), $y_{eff} = 0.5Z_\odot$, $\tau_1 = 6 \cdot \delta t$, and $\tau_2 = 7 \cdot \delta t$.

The example we show in Fig. 8 is meant only to be illustrative; other sets of parameters can be found similar to these which also give plausible deconstructions of the MDF. For an example of the accreting-box model applied to a still more distinct two-stage model, see Vandalsen & Harris (2004) and their discussion of bimodal MDFs for globular cluster systems. Several possible combinations of parameters are shown there, along with a nonlinear statistical procedure for finding the best-fitting parameters for an assumed model. Their discussion shows, however, that noticeably different model assumptions can lead to equally good combinations of model parameters, and the only way to select among these is through external physical constraints. The only clear constraint we have for the NGC 3379 data (within the context of the accreting-box models) is the empirically well defined changeover between modes at $Z \simeq 0.2Z_{\odot}$. Given this, we find that the final adopted y_{eff} is *internally* uncertain by ± 10 percent and the infall times τ_1, τ_2 by $\pm 2 \cdot \delta t$. For the abundance of the infalling gas, Z_{in} for the higher-metallicity mode needs to be within 10 percent of $Z_0 = 0.2Z_{\odot}$ to maintain the continuous transition between the two modes.

If interpreted at face value, the model shown above suggests that NGC 3379 underwent two fairly distinct epochs in its formation history. First was the buildup of a classic, metal-poor halo starting with pristine gas, a low effective yield, and without much “infall”, roughly resembling what we find in the Milky Way or in the dwarf ellipticals. We speculate that the end of this phase near $Z \simeq 0.2Z_{\odot}$ may, perhaps, be connected with the epoch of cosmological reionization that could have interrupted the first rounds of star formation in the pregalactic dwarf population around redshifts $z \sim 6 - 10$, including the metal-poor globular clusters (e.g. Santos 2003; Rhode et al. 2005). In this connection, Beasley et al. (2002) have noted that a truncation redshift quite similar to $z(reionization)$ is necessary to produce a distinctly bimodal MDF for globular clusters in their semianalytic model of galaxy formation.

The second major stage was the buildup of the metal-rich, bulge-like component (starting from gas that was pre-enriched from the first phase?) and with a higher effective yield. This second phase continued long enough for the star-forming gas to enrich up to Solar abundance or higher. The factor-of-five difference in y_{eff} between the two stages suggests that the “halo” star formation could have taken place in small potential wells (pregalactic clouds or dwarf-sized satellites) where a high fraction of the gas was lost to outflow; whereas the metal-richer component could be made within a deeper potential well that could hold on to much more of the gas. For comparison, in Harris & Harris (2002) we found $y_{eff} \simeq 0.3Z_{\odot}$ for the outer halo of NGC 5128 (a more massive giant than NGC 3379; see the Discussion section below), while for the inner region of NGC 5128, we found $y_{eff} \simeq 0.85Z_{\odot}$, which approaches the typical theoretically expected nucleosynthetic yield without gas loss.

We do not discuss here an alternate approach of building up the metal-poor component

of the halo completely by accretion of small, low-metallicity satellites at later times. Although there is clear evidence that these kinds of events are happening in the Milky Way and other large galaxies, evidence from the detailed abundance patterns of the heavy elements (which are different between the Milky Way halo stars and the dwarf spheroidal satellites; see Venn et al. 2004; Font et al. 2006; Pritzl et al. 2005) argues that the entirety of the halo did not build by late accretion.

The model shown in Fig. 8 also gives us a way to estimate the effects of photometric incompleteness on our measured MDF. If we extrapolate the same model past the observational cutoff $Z > 0.5Z_{\odot}$ out to $Z \sim 2Z_{\odot}$ (the upper limit suggested by Gregg et al. 2004), we should add another $\simeq 13\%$ to the entire population of stars in the diagram. Said differently, we would be missing about one-quarter of just the *metal-rich* component alone because of our photometric cutoff.

A more model-independent way to check this estimate of the numbers of very metal-rich stars is to look for stars on our original images that are well above our photometric limit in I , but below our cutoff in V . From the *allstar* file of measured objects in $F814W$, 1464 stars brighter than $I = 27$ were also measured in $F606W$, survived the cuts for $\chi_{V,I}$ and stellarity, and thus appeared in the final CMD. But in addition to these, there are $\simeq 260$ objects with $I \lesssim 27$ that were not matched successfully with anything in the $F606W$ image and thus could be very metal-rich RGB stars. These totals give an *upper limit* that our MDF could contain as many as 18% more stars beyond our photometric cutoff, entirely consistent with the model extrapolation described above. In summary, we do not appear to be missing a major part of the MDF at this location in the halo.

7. Comparison with Globular Clusters

The old-halo globular cluster (GC) population that is always present in E galaxies gives a second way to assess the metallicity distribution in the halo. Recent wide-field photometric studies of the GCs in NGC 3379 have been carried out by Whitlock, Forbes, & Beasley (2003) and Rhode & Zepf (2004) which verify earlier results that its GC population is quite small (unfortunately for our purposes). Rhode & Zepf (2004) estimate that the total GC population comprises only $N_{GC} \sim 270$ clusters, making the specific frequency (number of GCs per unit galaxy luminosity) $S_N = 1.2 \pm 0.3$. This level is 3 to 4 times lower than the average for typical large ellipticals in Virgo, Fornax, and other cluster environments, but not unlike at least some other ellipticals in the “field” and small groups (Harris 2001). Despite their small numbers, the GCs display the normal bimodal color and metallicity distribution that shows up almost universally in large galaxies (e.g. Harris 2001; Peng et al.

2006; Harris et al. 2006). Using the $(B - R)$ color index for a total of 36 well measured GCs, Rhode & Zepf (2004) deduce the presence of metal-poor and metal-rich subpopulations that are fairly distinct from each other. We have converted their $(B - R)$ histogram into $[\text{Fe}/\text{H}]$ with our own calibration based on 80 Milky Way globular clusters with low reddenings and measured colors (Harris 1996),

$$[\text{Fe}/\text{H}] = 3.13(B - R)_0 - 5.04 \quad (6)$$

along with $E_{B-R} = 0.04$ for NGC 3379. (Rhode & Zepf do the same to deduce the mean metallicities of each of the two modes, but do not quote the actual conversion relation they used.) We find that the blue GC mode is at $[\text{m}/\text{H}] \simeq [\text{Fe}/\text{H}] + 0.2 = -1.33$, and the red mode at $[\text{m}/\text{H}] \simeq -0.36$. Both of these mean points are internally uncertain to ± 0.2 dex. A double-Gaussian fit to the histogram shows that $\simeq 79\%$ of the GC population is in the blue mode and just 21% in the red mode, consistent with Rhode & Zepf’s estimates. The internal uncertainties in both the red and blue GC groups are high because of small-number statistics, though the red side is clearly the less certain of the two.

The natural question is to ask whether these two GC metallicity subgroups have any connection to the two-mode field-star MDF we discuss in the previous section. In Figure 9, we compare the two types of objects directly. For $[\text{m}/\text{H}] \lesssim -1$, the GC and RGB distributions match up well, consistent with the idea that the metal-poor clusters and field stars formed at the same time. If so, the continued formation of both may have been truncated at the same time (see discussion above). For the more metal-rich half of the MDF, the numbers of GCs are very much smaller and it is not yet clear whether their underlying distribution by metallicity has the same shape. It is notable, however, that the proportions of the two metallicity subgroups are very different, with the field halo including many more metal-rich objects relative to the metal-poor ones. This fundamental observed difference between the field stars and halo clusters is a type of “specific frequency problem” that appears to be quite a general issue in giant galaxies, and has not yet found a compelling explanation (see Harris 2001; Harris & Harris 2002; Beasley et al. 2003, for further discussion). The lowest-metallicity massive star clusters in some way formed at very high efficiency relative to the field stars.

A recent study of the GCs by Pierce et al. (2006) uses Gemini/GMOS spectra to measure ages, metallicities and abundance ratios for a sample of about two dozen GCs over the full range of metallicities. Although the sample size is small, they find that the clusters are uniformly old (> 10 Gyr), as is the case in the Milky Way.

The possibility that NGC 3379 is actually not a true elliptical, but a nearly face-on S0 galaxy, has been raised on the basis of the details of its light distribution (e.g. Capaccioli et al.

1991; Statler & Smecker-Hane 1999). Interestingly, the globular clusters provide some circumstantial evidence consistent with such an interpretation: the very low specific frequency $S_N \simeq 1.2$ would not be unusual for an S0 or a large disk galaxy, but is certainly on the extreme low end for true ellipticals. Another relevant piece of evidence is discussed by Pierce et al. (2006) and is based on kinematics. The planetary nebulae in the galaxy show a velocity dispersion that gradually declines with galactocentric distance (Romanowsky et al. 2003), whereas the velocity dispersion in the globular cluster system (Pierce et al. 2006) stays roughly constant with R_{gc} , as it would in a normal dark-matter halo with isotropic orbits. One way to reconcile the PN velocities with the GCs would be to suggest that the PNe have progressively increasing radial anisotropy outward. However, if the galaxy is an S0 that we see nearly face-on, the PNe might be more associated with a disklike population and thus have a lower dispersion along our line of sight, by contrast with the more spherically distributed GCs (see Pierce et al. 2006, for additional discussion).

8. The Metallicity Gradient

It is notable that the inner halo fields studied with *NICMOS* by Gregg et al. (2004) showed no significant numbers of low-metallicity stars, whereas our outer-halo field shows a large number of them. This comparison, and the chemical evolution argument made in the previous section, suggests that we should look more closely for traces of a *metallicity gradient*. Fortunately, the $200''$ width of the ACS/WFC field is large enough to span a radial range 27.7 kpc to 38.1 kpc from the center of NGC 3379. Across this one field, do we see any changes in the relative numbers of metal-poor and metal-rich stars?

The answer is yes. In Figure 10, we show the positions of the brighter ($26 < I < 27.3$) measured stars on the image, where we have subdivided them into the same two major groups that were identified from the entire MDF: a “blue” metal-poor population with $Z < 0.2Z_\odot$ ($[m/H] < -0.7$), and a “red” group with $Z > 0.2Z_\odot$. The blue group includes the obvious dE-like RGB that defines the low-metallicity half of the chemical evolution model in Fig. 8. Recall that the upper part of the image (large y -values) is the east side of the frame, closest to NGC 3379. For the red group, a very obvious density gradient appears, while the blue group is more evenly spread.

We show these two subpopulations again in Figure 11, plotted as the number density σ of stars per unit area as a function of position y or, alternately, projected radius R_{gc} from the center of the galaxy. Approximate power-law profiles can be matched to each one, but it is the difference between the two that is striking. The blue RGB is well described by $\sigma \sim R^{(-1.2 \pm 0.7)}$, whereas the red RGB population needs a much steeper gradient near

$\sigma \sim R^{(-6.0 \pm 0.6)}$ to match the data.³ For both groups combined, the overall gradient is $\sigma \sim R^{-4.5 \pm 0.5}$.

The large-scale surface brightness (SB) distribution of the galaxy, with the ACS field position marked on it, is shown in Figure 12. The standard $r^{1/4}$ profile determined by de Vaucouleurs & Capaccioli (1979) and extended by Capaccioli et al. (1990) is $\mu_B = 14.076 + 3.0083R^{1/4}$ for R in arcseconds and μ_B in mag/arcsec²; note, however, that for $\mu_B > 28$ the measurements are quite uncertain (see Capaccioli et al. 1990). At our field position of $r \simeq 650''$, we expect $\mu_B \simeq 29.3$. Replotted as surface brightness versus $\log R$, a straight line in μ versus $R^{1/4}$ takes on a steadily steeper logarithmic slope for increasing R , and at our field position, the profile would predict that the surface brightness should vary approximately as $I \sim R^{-6}$, consistent with the power-law exponent that we observe for the red RGB stars.

A third way of representing the metallicity gradient is shown in Figure 13. Here, we plot CMDs separately for the upper half ($y > 2000$ px, eastern side) and the lower half ($y < 2000$ px, western side). The west side, which is the one further from the center of NGC 3379, has far fewer metal-rich giants, and its CMD begins to resemble rather closely that of a typical metal-poor dwarf elliptical (Han et al. 1997; Butler & Martinez-Delgado 2005).

Our data indicate that at radii $R \lesssim 500''$ the starcounts (and thus the halo surface brightness) should be completely dominated by the higher-metallicity stars. These are what we see in the published SB profile. However, if the SB measurements could be extended accurately outward beyond $R > 800''$, we should see a flattening of the profile to something closer to $I \sim R^{-2}$ or even less as the metal-poor component takes over. Surface brightness measurements at such low levels are exceptionally difficult, however, and the most effective way to continue them outward is likely to be precisely the method we have used here: that is, through starcounts of the resolved RGB population.

The presence of a metallicity gradient also allows us to reconcile our data rather easily with those of Gregg et al. (2004): if the metal-rich component rises inward as steeply as we see it do, then their inner-halo CMDs should have been dominated by high-metallicity stars, as in fact they are. The small *NICMOS* field and thus the smaller absolute numbers of stars tends to exaggerate their prominence as well. If we use the power laws from Fig.11 to scale the expected number densities of the bluer and redder RGB components from the inner edge of our ACS field at $R = 9.3'$ inward to (e.g.) the middle *NICMOS* field at $R = 4.5'$, then we would predict that the redder RGB stars should outnumber the bluer ones at the same

³To determine these radial curves we select stars in the range $I < 27.3$. It should be noted that this is not the same limit as used above for the MDF, and the total numbers of stars in each group should thus not be compared. We use the latter magnitude cut only to estimate the radial slopes.

limiting I luminosity by at least 10 to 1 there, making them very hard to detect. In fact, such a scaling is likely to be extremely uncertain since it does not account for the flattening off of the surface brightness profile of either component (see again Fig. 12). Gregg et al. (2004) suggest that they find a small metal-poor component amidst the dominant metal-rich one, but this conclusion rests heavily on an extremely accurate understanding of their photometric uncertainties in the faintest 1 mag of their data (see their Fig. 12). The best way to determine the true radial profile of the intriguing metal-poor component will be by further deep observations at selected and widely spaced radii.

Lastly, in Figure 14 we show a direct comparison between the two MDFs in the eastern and western halves of our field. In the upper panel of the Figure, the two are superimposed on each other, but normalized to the same *total* number of stars more metal-poor than a rather arbitrarily chosen dividing line at $[m/H] = -1$. When normalized this way, the eastern half has an excess of metal-rich stars, shown in the lower panel which plots the difference between the two halves. The excess metal-rich component must have a mean metallicity of at least $\langle m/H \rangle > -0.5$, typical of the bulges or disks of large galaxies. We can set only a lower limit to it, since a significant fraction of it is likely to extend above our photometrically imposed cutoff near $[m/H](\text{max}) \simeq -0.2$.

Our choice of field location turns out to be more fortunate than we initially anticipated. It is, apparently, *just* at the radial range that we study in which the metal-rich component is rapidly dying out, and in which the metal-poor halo is starting to emerge clearly from underneath it. We have been able to see both components at once. If we had selected a field pointing $\sim 3' - 5'$ either farther out or farther in, our CMD would have been dominated by only one of these components and the nature of the population gradient would not have been as clear. The shallow surface density dependence $\sigma \sim R^{-1.2 \pm 0.7}$ of the metal-poor halo component is, if anything, even flatter than that expected for an NFW potential well, which should converge to a projected density $\sigma \sim R^{-2}$ in its outer regions (Navarro et al. 1997), although the difference is within the uncertainty of measurement. The slope would be at least roughly consistent with the idea (see above) that the low-metallicity stars formed in pregalactic clouds that were widely dispersed within the dark-matter halo before the main epoch of hierarchical merging and dissipative collapse.

A last bit of evidence worth noting is that the metal-rich *globular clusters* (discussed in the previous section) have a different spatial distribution than the metal-poor clusters. The data from Rhode & Zepf (2004) (see their Fig. 10) show that no red GCs are found beyond $R_{gc} \simeq 12'$, just at the radial distance of our ACS field where we see the metal-rich RGB stars rapidly declining. By contrast, the blue GCs continue on outward detectably to $R_{gc} > 20'$ (60 kpc). This comparison is consistent with the often-expressed view (e.g. Harris

2001; Beasley et al. 2003; Harris & Harris 2002) that the metal-rich GCs formed with the bulk of the gE that is predominantly metal-rich.

Our data from NGC 3379, however, add new evidence to support the complementary view that the *metal-poor stars and GCs* both belonged to an earlier stage at which the protogalactic gas clouds were more widely distributed. What remains unexplained about this epoch is the relatively large proportion of GCs to metal-poor halo stars.

If in fact the galaxy is actually a nearly face-on S0 rather than an E1 (see above), our interpretation would have to be modified to the view that the moderately metal-rich *disk* component dies out steeply near our field location, again leaving the metal-poor halo to continue outward.

9. Discussion

In other large E galaxies for which MDFs have been derived based on *direct photometry of halo stars*, no radial metallicity gradients in the MDFs have been seen. What distinguishes NGC 3379 from these others?

The most obvious possibility to raise is that, in these other systems, the existing photometry has not reached far enough out into the halo *relative to the effective radius of the spheroid*. In NGC 3379, the transition from metal-rich dominance to metal-poor dominance occurs at the R_{gc} range from $10R_e$ to $13R_e$, where the effective radius is $R_e = 0'.93 = 2.8$ kpc. For NGC 5128, the four fields studied so far range from $1.4R_e$ to $7.3R_e$ ($R_e = 5.5$ kpc); and for NGC 3377, the field surveyed covers $1.5R_e$ to $5.3R_e$ ($R_e = 3.3$ kpc). Thus in NGC 3379 we have sampled the halo about twice as far out *in units of R_e* as in these other systems.

The most directly comparable observations in the literature may instead come from those of a giant *disk* galaxy, M31. Several recent studies have begun to trace the stellar density distribution and metallicity distribution of the M31 stars outward as far as $R = 165$ kpc in projected radius (Irwin et al. 2003; Guhathakurata et al. 2006; Kalirai et al. 2006, and references cited there). For $R \lesssim 30$ kpc, the MDF is moderately metal-rich, like those in the large ellipticals we have discussed above, and with no obvious metallicity gradient. Beyond $R \sim 60$ kpc, however, the MDF becomes much more metal-poor with a mean near $[\text{Fe}/\text{H}] \simeq -1.3$ to -1.5 that resembles the Milky Way halo (Kalirai et al. 2006). These authors state that the “transition zone” between a bulge-like metal-rich population and the metal-poor halo starts near 30 kpc. Since $R_e = 4.7$ kpc for M31 ($R_e = 20'.8$ from RC3), their conclusion is essentially that the “pure halo” component becomes dominant only for $R \gtrsim 10R_e$, entirely consistent with what we have found. In addition, the fact that no metallicity gradient shows

up for either $R < 30$ kpc or $R > 60$ kpc indicates that the two components are each fairly homogeneous, and that the overall metallicity gradient is the result of changing proportions of the two with radius. We invite the reader to compare Kalirai et al.’s color-magnitude diagram (their Figure 6) with our Figure 5: even though there are far fewer stars in their M31 diagram, its overall pattern relative to the grid of RGB isochrones strongly resembles what we find for NGC 3379.

A more well known galaxy with an extended metal-poor halo is of course the Milky Way. The spatial distribution for metal-poor stars and globular clusters follows a three-dimensional profile $\phi \sim r^{-a}$ where $a \simeq 3.0 - 3.5$ (Harris 2001; Kinman et al. 1994; Sluis & Arnold 1998; Maintz & deBoer 2005) and continues outward well past $r > 50$ kpc, similar to what we are beginning to find specifically for M31 and NGC 3379. In a few other nearby disk galaxies that are edge-on, evidence for low-metallicity, very low-density halos is also now beginning to emerge (e.g. Seth et al. 2007; Tikhonov et al. 2006) with the same method of resolved stellar photometry. These studies are finding that the halo component becomes noticeable at heights of $\simeq 5$ kpc or more above the disk plane. If these metal-poor haloes are common features of galaxies, they mostly likely have remained undetected until recent years simply because of their extremely low surface brightnesses at large galactic radii. For example, in the Milky Way, the metal-poor halo has $\mu = 30$ mag arcsec $^{-2}$ at the Solar radius (Binney & Merrifield 1998), a level of faintness that is extremely challenging even for the most meticulous surface-brightness photometry. The alternate route (at least for nearby galaxies) of resolved-star photometry can reach much fainter equivalent levels.

Yet another, though more indirect, window into the outer-halo stellar populations of galaxies may be found in the intracluster stellar light found in clusters of galaxies. These free-floating stars, unbound to any particular member galaxy, are stripped from infalling galaxies during tidal interactions. Murante et al. (2004) find that not only do intracluster (IC) stars *not* represent a random sampling from cluster galaxies, but that they tend to be older than bound stars, a result supported by Sommer-Larsen et al. (2005). Willman et al. (2004) also find an age disparity between their bound and unbound stellar populations, and in their simulations of galaxy clusters, they trace the origin of stars that end up in the intracluster population. They find that galaxies of all sizes contribute stars to the ambient IC population and that stars are preferentially pulled from the outer and lower-metallicity parts of their stellar distributions. Although a study of Virgo IC stars by Durrell et al. (2002) finds stars of predominantly intermediate metallicity, there is evidence of substantial structure in the IC light in Virgo (Mihos et al. 2005) and its unbound stellar populations are most likely not yet well-mixed.

Williams et al. (2007) obtained ACS data on an intracluster field in Virgo, and find an

MDF roughly similar to ours. A comparison of our Fig.5 with the CMD in their Figure 7 reveals that the metallicity distribution of these Virgo cluster stars is rather similarly spread over the full abundance range. Williams et al. (2007) argue that a noticeable proportion of younger stars is present in this sample in addition to a basic old population with a broad MDF. While some mixing is expected in the IC population, the fact that this intracluster MDF resembles those in the outer halos of NGC 3379 and M31 might itself be indirect evidence that large galaxies in general possess metal-poor halos, because the tidally stripped material will come preferentially from those outer parts of large and intermediate galaxies.

A comparison of halo-star MDFs in E galaxies, from dwarfs to giants, can now be made and is shown more explicitly in Figure 15. These include: the Local Group dwarf spheroidals Draco ($M_V^T = -8.8$; Mateo 1998) and Leo I ($M_V^T = -11.9$), with spectroscopic and photometric metallicity data from Faria et al. (2007) and Koch et al. (2007); the Local Group dwarf NGC 147 ($M_V^T = -15.6$), with photometric (V, I) RGB data from Han et al. (1997); the intermediate-luminosity Leo member NGC 3377 (Harris et al. 2007); our data for NGC 3379; and the outermost NGC 5128 halo fields at $R_{gc} = 40$ kpc (Rejkuba et al. 2005). We use Draco and Leo I only as representative cases of dwarf spheroidals that allow us to exhibit as large as possible a range of host galaxy sizes. In the latter four cases, exactly the same interpolation code and RGB model grid has been used to derive the MDF. For the two dwarf spheroidals, with very low luminosities and distinctly lower mean metallicities than the others, the MDFs are as presented in the papers cited above. The galaxies are shown in order of increasing total luminosity. Note, in particular, that NGC 5128 is a giant twice as massive as NGC 3379; dynamical mass measurements to comparably large radii give $M \simeq 4 \times 10^{11} M_\odot$ for NGC 3379 (Bergond et al. 2006) and $M \simeq 10 \times 10^{11} M_\odot$ for NGC 5128 (Woodley et al. 2007).

The sequence in Fig. 15 clearly shows up as a progressively increasing mean heavy-element abundance (keeping in mind that both the NGC 3377 and NGC 3379 data are truncated by photometric incompleteness for $Z > 0.6Z_\odot$ and that the true numbers of stars at Solar metallicity and beyond are not accurately known). By contrast, the other four galaxies are more deeply sampled and less affected by incompleteness. A secondary feature worth noting is the shape of the MDF at very low Z in NGC 147 and 3377, in which the number of stars per unit Z rises steeply for $Z < 0.1Z_\odot$ before turning over and declining. This MDF feature at low Z can easily be interpreted as a signature of infall of primordial, relatively unenriched gas during the earliest stages of star formation. By contrast, the low- Z end of the NGC 3379 MDF has relatively much larger numbers of stars, closely matching a closed-box model with no need to invoke infall (see discussion above). This MDF would be consistent with rapid very early formation, even before the major stages of hierarchical merging began. But it is not yet clear how much of this difference in MDF shape between

NGC 3379 and the other galaxies could be due to the rather different locations in the halo that each one has been studied, and whether or not the metal-rich and metal-poor subcomponents that we propose actually do belong to different evolutionary stages.

The sequence of host galaxies shown in Fig. 15 allows us to exhibit almost the entire observable range of E galaxy types, with potential-well masses from $\sim 10^7 M_\odot$ up to $10^{12} M_\odot$. We miss only the “supergiant” or cD-type galaxies with still higher masses. Nevertheless, the sequence we can now put together from existing data already covers a large dynamic range. In our simple chemical evolution model, the location of the peak or mode of the MDF in the sequence shown is determined by the effective yield y_{eff} . The observable trend for y_{eff} to increase systematically with the depth of the host potential well of the galaxy as a whole, is highly suggestive of the ability to hold onto the gas in the region through many successive rounds of star formation, which is expected to be larger in the more massive galaxies.

It remains to ask what the origin of the *low-metallicity*, diffuse halo component is likely to be. Buildup of the outer halo by accretion of metal-poor satellite dwarfs is a much-discussed option, especially since traces of such events are being found for the Milky Way and M31 (Majewski 1993; Majewski et al. 1996; Newberg et al. 2002; Ibata et al. 2005; Guhathakurata et al. 2006, among many others). Part of the evidence for such accretion events involves the presence of tidal streams, clumps, and overall patchiness of the light distribution. The smoothness and regularity of the halo profile around NGC 3379 may therefore argue against accretion, unless most of these events happened so long ago that all such features have had time to diffuse completely. However, in that case the semantic distinction between halo buildup by accretion, versus an ordinary sequence of early hierarchical merging, becomes somewhat blurred (e.g. Bekki & Chiba 2001).

The formation of large E galaxies by major mergers of disk galaxies is also a well established interpretation. In such mergers, the majority of the halo stars in the merged product are the moderately metal-rich stars in the former disks of the progenitor galaxies, which can be launched out to large radii (e.g. Bekki et al. 2003) and leave an extended halo with little overall metallicity gradient. However, these merger models also indicate that at very large radii (40 kpc and beyond), the metal-rich component should die away and the “true” metal-poor halo stars of the progenitor disk galaxies should become relatively more noticeable (see Bekki et al. 2003).

The possible role of formation by the more conventional route of dissipational collapse, starting from a widely spread distribution of primordial gas clouds, should not be ignored. Existing dissipative-collapse models (e.g. Angeletti & Giannone 2003, for a recent representative example applied to E galaxies) are, however, pointed at recovering the metallicity gradients that are observed in the brightest inner halos and bulges of E galaxies (e.g.

Davies et al. 1993), which should arise during the main stage of the bulge and spheroid formation. The remote, metal-poor regions could have an earlier origin. A broad-based simulation for disk-galaxy formation which includes the large-scale halo (Bekki & Chiba 2001) suggests that its outskirts were formed by a combination of dissipative collapse and accretion of satellites, leaving a present-day halo with a roughly spherical distribution and a projected radial profile slope $a \simeq 2.5$. As noted earlier, the expected slope at large radius might be $a \simeq 2$, the profile of the dark-matter potential well (Navarro et al. 1997).

Much more observational work can obviously be done to test the ideas discussed above, both in the nearest systems such as NGC 5128 and the Leo galaxies, and in other systems. Our prediction is essentially that large galaxies in general will reveal extensive, metal-poor halos that become the dominant component at scale radii $R \gtrsim 12R_e$. Additional tests of the stellar number densities and MDFs at different radii in these same galaxies would be of great interest. Another set of target galaxies that would in many ways be optimum for this type of deep, metallicity-sensitive stellar photometry would be the Virgo cluster galaxies at $d = 16$ Mpc. Virgo holds the largest collection of E galaxies of all types in the local universe, and at just one magnitude more distant than the Leo group, their red-giant halo stars will be within reach of the HST ACS and WFC3 cameras without prohibitively long exposure times (Williams et al. 2007). In the search for the extended metal-poor halos in giant galaxies that might represent their earliest formation stages, however, attention should also be paid to relatively more isolated systems where there will be less concern about confusion from intracluster stellar light generated by later dynamical evolution. It is clear that with the right tools, this observational field is just beginning.

10. Summary

We have used deep HST/ACS images of an outer-halo field in the giant elliptical galaxy NGC 3379, a central member of the Leo group, to derive the metallicity distribution function of its old red-giant stars. A total of 5300 stars were measured over a radial region extending from 9.2 to 12.7 (equivalent to 28 to 38 kpc, or 9.9 to 13.6 R_e) projected distance from the galaxy center. The (V, I) data reach deep enough to reveal almost 2 magnitudes of the red-giant branch and show what appears to be a purely old population with little evidence for younger stars.

The MDF for this region of the halo shows two major features that make it distinctly unlike other E/S0 galaxies including the Local Group dwarf ellipticals, the intermediate-luminosity Leo member NGC 3377, and the Centaurus giant NGC 5128: first, the MDF for the NGC 3379 halo is extremely broad and flat, with many stars at every interval in

$[m/H]$ and only a gradual rise towards higher metallicity. Second, a *metallicity gradient* is clearly detectable across our ACS field. The higher-metallicity stars ($[m/H] > -0.7$) fall off steeply as $\sigma \sim R^{-6.0}$, while the lower-metallicity component shows a much shallower profile $\sigma \sim R^{-1.2}$. We suggest that our target field is just at the transition point where, in essence, the high-metallicity component of the galaxy reaches its edge and the shallower lowest-metallicity component becomes the dominant one by default.

In order to successfully match this extremely broad MDF, we find that a distinct two-stage accreting-box chemical evolution model is necessary, whereby the metal-poor, diffuse halo belonged to a rapid initial formation phase strongly resembling a simple closed-box model with very low effective yield $y_{eff} \simeq 0.1Z_{\odot}$ and truncated at abundance $Z \simeq 0.2Z_{\odot}$. By contrast, the metal-rich component (the centrally concentrated spheroid or, possibly, the nearly face-on disk if NGC 3379 is actually an S0) requires an accreting-box type of model and an effective yield 5 times higher.

Our target field is at $R = 12R_e$, twice as far out in units of effective radius as in any of the other galaxies that we have surveyed with this technique of deep stellar photometry. We believe that this is the key factor allowing us to see the transition point between the metal-rich spheroid and the more extensive and sparser metal-poor halo. Some support for this view comes from the recent observations of the outer halo of M31, in which a metal-poor halo also emerges past $\sim 10R_e$. If NGC 3379 is indeed a representative case, we predict that large E/S0 galaxies *in general* will have diffuse, very low-metallicity halo components, but that photometry at radii $R \simeq 10 - 15R_e$ will be necessary to find them.

Finally, we summarize a series of arguments pointing to the possibility that NGC 3379 may be an S0 galaxy rather than an E1. These arguments involve the internal dynamics and isophotal contours, the globular cluster specific frequency, and the kinematic difference between the globular clusters and the planetary nebulae. None of these bits of evidence are individually strong, however, and the possibility remains ambiguous.

WEH, GLHH, and EMHW thank the Natural Sciences and Engineering Research Council of Canada for financial support. ACL acknowledges Support for this work through grant number HST-GO-09811.01-A from the Space Telescope Science Institute. We are indebted to James Taylor and Hugh Couchman for instructive conversations.

REFERENCES

Angeletti, L., & Giannone, P. 2003, A&A, 403, 449

- Bahcall, J., & Soneira, R. 1981, *ApJS*, 47, 357
- Beasley, M.A., Baugh, C.M., Forbes, D.A., & Sharples, R.M. 2002, *MNRAS*, 333, 383
- Beasley, M.A., Harris, W.E., Harris, G.L.H., & Forbes, D.A. 2003, *MNRAS*, 340, 341
- Bekki, K., & Chiba, M. 2001, *ApJ*, 558, 666
- Bekki, K., Harris, W.E., & Harris, G.L.H. 2003, *MNRAS*, 338, 587
- Bekki, K., & Peng, E.W. 2006, *MNRAS*, 370, 1737
- Bellazzini, M., Ferraro, F.R., Sollima, A., Pancino, E., & Origlia, L. 2004, *A&A*, 424, 199
- Bergond, G., Zepf, S.E., Romanowsky, A.J., Sharples, R.M., & Rhode, K.L. 2006, *A&A*, 448, 155
- Bertin, E., & Arnouts, S. 1996, *A&AS*, 117, 393
- Binney, J., & Merrifield, M. 1998, *Galactic Astronomy* (Princeton: Princeton Univ. Press)
- Butler, D.J., & Martinez-Delgado, d. 2005, *AJ*, 129, 2217
- Capaccioli, M., Held, E.V., Lorenz, H., & Vietri, M., 1990, *AJ*, 99, 1813
- Capaccioli, M., Vietri, M., Held, E.V., & Lorenz, H. 1991, *ApJ*, 371, 535
- Carroll, B.W., & Ostlie, D.A. 2007, *An Introduction to Modern Astrophysics* (San Francisco: Pearson Addison-Wesley), Chp 25
- Ciardullo, R., Jacoby, G.H., & Ford, H.C. 1989, *ApJ*, 344, 715
- Davies, R.L., Sadler, E.M., & Peletier, R.F. 1993, *MNRAS*, 262, 650
- de Vaucouleurs, G., & Capaccioli, M. 1979, *ApJS*, 40, 699
- Durrell, P.R., Ciardullo, R., Feldmeier, J.J., Jacoby, G.H., & Sigurdsson, S. 2002, *ApJ*, 570, 119
- Faria, D., Feltzing, S., Lundstrom, I., Gilmore, G., Wahlgren, G.M., Ardeberg, A., & Linde, P. 2007, *A&A*465, 357
- Ferrarese, L., Côté, P., Jordán, A., Peng, E.W., Blakeslee, J.P., Piatek, S., Mei, S., Merritt, D., Milosavljevi, M., Tonry, J.L., & West, M.J. 2006, *ApJS*, 164, 334
- Fleming, D.E.B., Harris, W.E., Pritchett, C.J., & Hanes, D.A. 1995, *AJ*, 109, 1044

- Font, A.S., Johnston, K.V., Bullock, J.S., & Robertson, B.E. 2006, *ApJ*, 638, 585
- Gregg, M.D., Ferguson, H.C., Minniti, D., Tanvir, N., & Catchpole, R. 2004, *AJ*, 127, 1441
- Grillmair, C.J. et al. 1996, *AJ*, 112, 1975
- Guhathakurta, P., Rich, R.M., Reitzel, D.B., Cooper, M.C., Gilbert, K.M., Majewski, S.R., Ostheimer, J.C., Geha, M.C., Johnston, K.V., & Patterson, R.J. 2006, *AJ*, 131, 2497
- Han, M. et al. 1997, *AJ*, 113, 1001
- Harris, G.L.H., Harris, W.E., & Poole, G.B. 1999, *AJ*, 117, 855
- Harris, G.L.H., & Harris, W.E. 2000, *AJ*, 120, 2423
- Harris, W.E. 1996, *AJ*, 112, 1487
- Harris, W.E. 2001, in *Star Clusters, Saas-Fee Advanced Course 28* (New York: Springer), ed. L.Labhardt & B.Binggeli
- Harris, W.E., & Harris, G.L.H. 2002, *AJ*, 123, 3108
- Harris, W.E., Harris, G.L.H., Layden, A.C., & Stetson, P.B. 2007, *AJ*, 134, 43
- Harris, W.E., Whitmore, B.C., Karakla, D., Okón, W., Baum, W.A., Hanes, D.A., & Kavelaars, J.J. 2006, *ApJ*, 636, 90
- Ibata, R., Chapman, S., Ferguson, A.M.N., Lewis, G., Irwin, M., & Tanvir, N. 2005, *ApJ*, 634, 287
- Irwin, M.J., Ferguson, A.M.H., Ibata, R.A., Lewis, G.F., & Tanvir, N.R. 2003, *ApJ*, 628, L105
- Israel, F.P. 1998, *A&A Rev.*, 8, 237
- Kalirai, J.S., Gilbert, K.M., Guhathakurta, P., Majewski, S.R., Ostheimer, J.C., Rich, R.M., Cooper, M.C., Reitzel, D.B., & Patterson, R.J. 2006, *ApJ*, 648, 389
- Kinman, T.D., Suntzeff, N.B., & Kraft, R.P. 1994, *AJ*, 108, 1722
- Koch, A., Wilkinson, M.I., Kleyana, J.T., Gilmore, G.F., Grebel, E.K., Mackey, A.D., Evans, N.W., & Wyse, R.F.G. 2007, *ApJ*, 657, 241
- Maintz, G., & de Boer, K.S. 2005, *A&A*, 442, 229

- Majewski, S.R. 1993, *ARA&A*, 31, 575
- Majewski, S.R., Munn, J.A., & Hawley, S.L. 1996, *ApJ*, 459, L73
- Malin, D.F., Quinn, P.J., & Graham, J.A. 1983, *ApJ*, 272, L5
- Marleau, F.R., Graham, J.R., Liu, M.C., & Charlot, S. 2000, *AJ*, 120, 1779
- Mateo, M. 1998, *ARA&A*, 36, 435
- Mihos, J.C., Harding, P., Feldmeier, J., & Morrison, H. 2005, *ApJ*, 631, L41
- Murante, G., Arnaboldi, M., Gerhard, O., Borgani, S., Cheng, L.M., Diaferio, A., Dolag, K., Moscardini, L., Tormen, G., Tornatore, L., & Tozzi, P. 2004, *ApJ*, 607, L83
- Navarro, J.F., Frenk, C.S., & White, S.D.M. 1997, *ApJ*, 490, 493
- Newberg, H.J. et al. 2002, *ApJ* 569, 245
- Pagel, B.E.J., & Patchett, B.E. 1975, *MNRAS*, 172, 13
- Peng, E.W., Ford, H.C., Freeman, K.C., & White, R.L. 2002, *AJ*, 124, 3144
- Peng, E.W. et al. 2006, *ApJ*, 639, 95
- Pierce, M. et al. 2006, *MNRAS*, 366, 1253
- Prantzos, N. 2003, *A&A*, 404, 211
- Pritzl, B.J., Venn, K.A., & Irwin, M. 2005, *AJ*, 130, 2140
- Quillen, A.C., Graham, J.R., & Frogel, J.A. 1993, *ApJ*, 412, 550
- Rejkuba, M., Greggio, L., Harris, W.E., Harris, G.L.H., & Peng, E.W. 2005, *ApJ*, 631, 262
- Renzini, A. 1998, *AJ*, 115, 2459
- Rhode, K.L., & Zepf, S.E. 2004, *AJ*, 127, 302
- Rhode, K.L., Zepf, S.E., & Santos, M.R. 2005, *ApJ*, 630, L21
- Romanowsky, A.J., Douglas, N.G., Arnaboldi, M., Kuijken, K., Merrifield, M.R., Napolitano, N.R., Capaccioli, M., & Freeman, K.C. 2003, *Sci*, 301, 1696
- Sakai, S., Madore, B.F., & Freedman, W.L. 1996, *ApJ*, 461, 713

- Sakai, S., Madore, B.F., Freedman, W.L., Lauer, T.R., Ajhar, E.A., & Baum, W.A. 1997, *ApJ*, 478, 49
- Salaris, M., Cassisi, S., & Weiss, A. 2002, *PASP*, 114, 375
- Santos, M.R. 2003, in *Extragalactic Globular Cluster Systems*, ed. M. Kissler-Patig (New York: Springer), 348
- Schweizer, F., & Seitzer, P. 1992, *AJ*, 104, 1039
- Seth, A., De Jong, R., Dalcanton, J., & the GHOSTS Team 2007, in *IAU Symposium 241, Stellar Populations as Building Blocks of Galaxies* (astro-ph/0701704)
- Shapiro, K.L., Cappellari, M., de Zeeuw, T., McDermid, R.M., Gebhardt, K., van den Bosch, R.C.E., & Statler, T.S. 2006, *MNRAS*, 370, 559
- Sluis, A.P.N., & Arnold, R.A. 1998, *MNRAS*, 297, 732
- Sommer-Larsen, J., Romeo, A. D., & Portinari, L. 2005, *MNRAS*, 357, 478
- Statler, T.S., & Smecker-Hane, T. 1999, *AJ* 117, 839
- Tikhonov, N.A., Galazutdinova, O.A., & Drozdovsky, I.O. 2006, *A&A*(astro-ph/0603457)
- Tonry, J.L., Dressler, A., Blakeslee, J.P., Ajhar, E.A., Fletcher, A.B., Luppino, G.A., Metzger, M.R., & Moore, C.B. 2001, *ApJ*, 546, 681
- Tubbs, A.D. 1980, *ApJ*, 241, 969
- VanDalsen, M.L., & Harris, W.E. 2004, *AJ*, 127, 368
- VandenBerg, D.A., Swenson, F.J., Rogers, F.J., Iglesias, C.A., & Alexander, D.R. 2000, *ApJ*, 532, 430
- Venn, K.A., Irwin, M., Shetrone, M.D., Tout, C.A., Hill, V., & Tolstoy, E. 2004, *AJ*, 128, 1177
- Whitlock, S., Forbes, D.A., & Beasley, M.A. 2003, *MNRAS*, 345, 949
- Williams, B.F. et al. 2007, *ApJ*, 656, 756
- Willman, B., Governato, F., Wadsley, J., & Quinn, T. 2004, *MNRAS*, 355, 159
- Woodley, K.A. 2006, *AJ*, 132, 2424

Woodley, K.A., Harris, W.E., Beasley, M., Peng, E.W., Bridges, T.J., Forbes, D.A., & Harris, G.L.H. 2007, AJ, in press (astro-ph/0704.1189)

Table 1. Basic Parameters for NGC 3379

Parameter	Value
<i>Type</i>	E1
α (J2000)	$10^h47^m49^s.6$
δ (J2000)	$12^\circ34'54''$
v_r (helio)	911 km s^{-1}
A_V	0.08
$(m - M)_0$	30.06 ± 0.10
V_T^0	9.20
M_V^T	-20.85

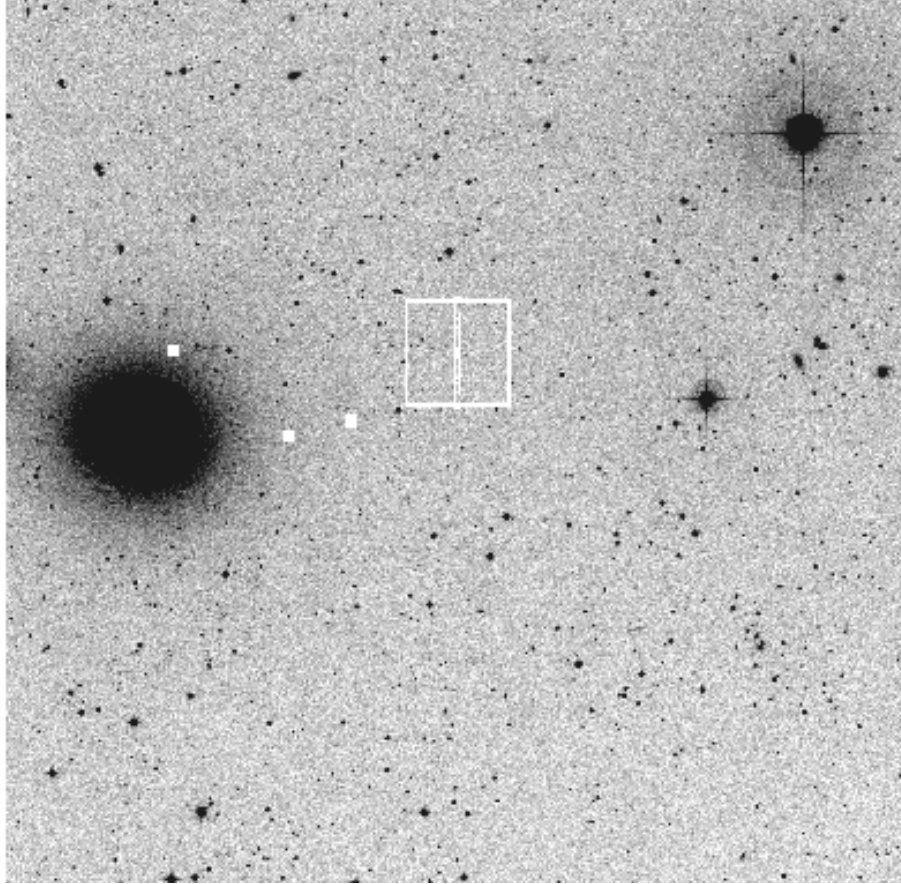


Fig. 1.— A wide-field image of the area containing our target field, extracted from the Digital Sky Survey. The bright galaxy near the left edge is NGC 3379 and the entire field is $30'$ across; North is at top and East at left. Our ACS/WFC field is marked by the large box at the center of the frame; the vertical bar through the middle shows the orientation of the gap between the two WFC CCD detectors. The three solid dots between NGC 3379 and the ACS field show the locations of the three NICMOS fields observed by Gregg et al. (2004). The WFPC2 field imaged in I by Sakai et al. (1997) is centered on the outermost of the three NICMOS fields.

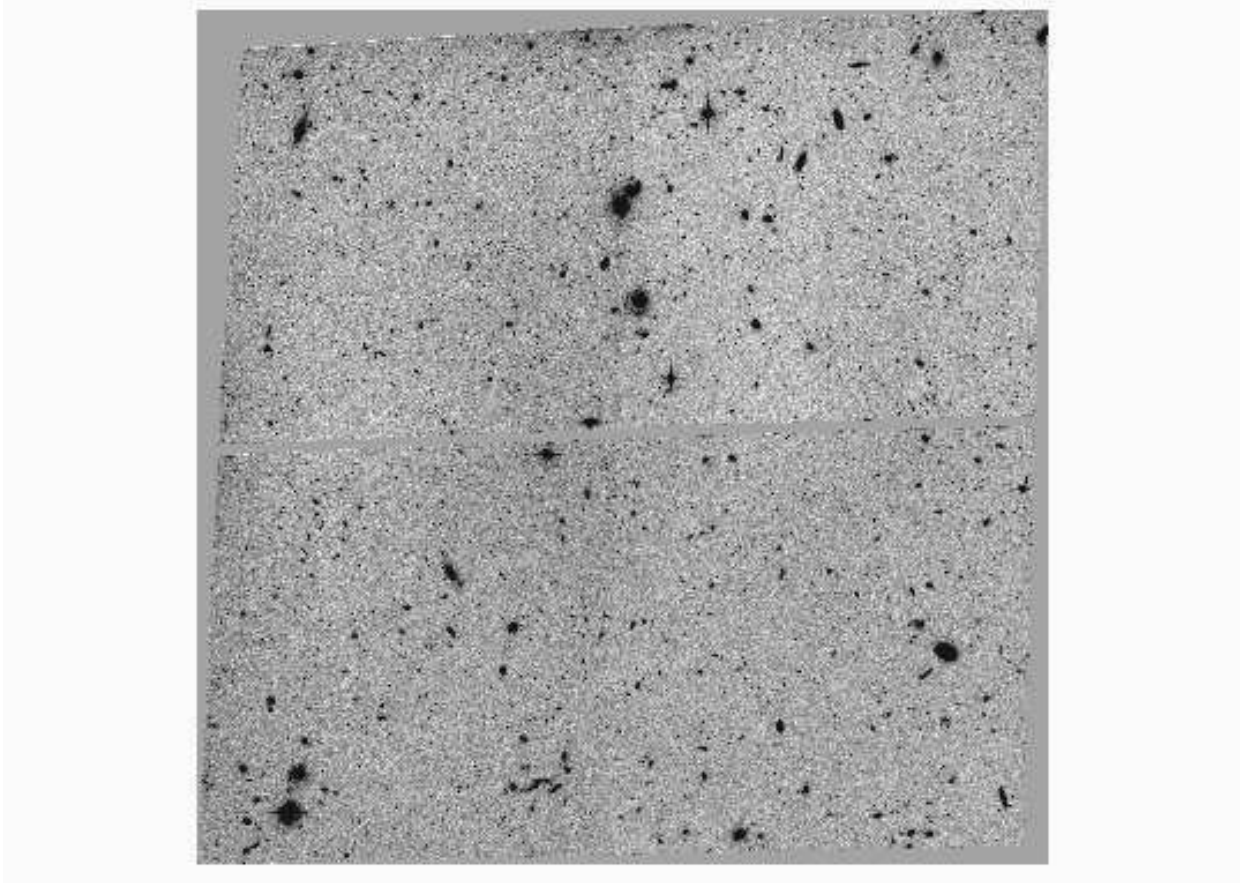


Fig. 2.— A reproduction of our ACS Wide Field Channel field. The orientation of this field is rotated nearly at right angles relative to the previous wide-field image; here, North is at the right and East at top. The y -axis of the ACS is directed 96° E of N. Notice the large number of background galaxies, which are the dominant source of field contamination (see text).

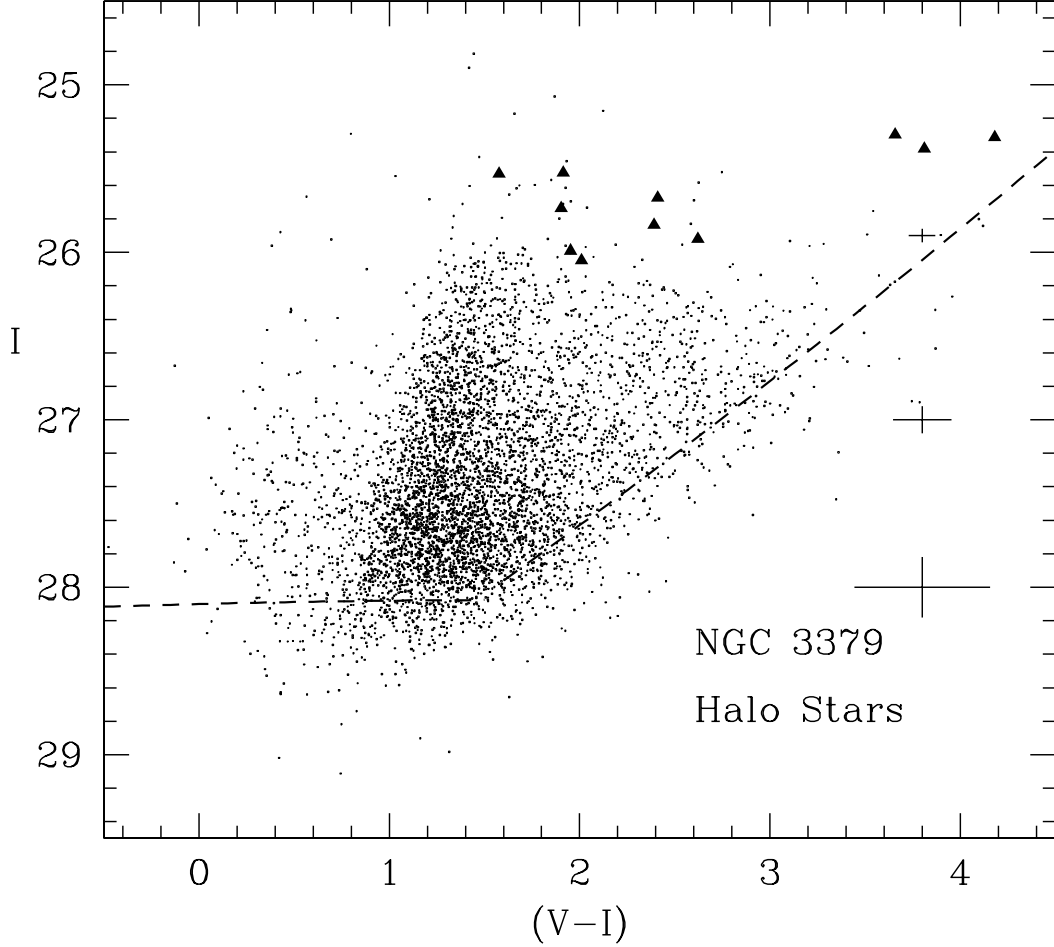


Fig. 3.— The color-magnitude array in $I, (V - I)$ for our measured sample of 5323 stars in the halo of NGC 3379. The dashed lines show the 50% detection completeness limits in I (horizontal line at bottom) and V (line sloping upward to the right). The errorbars shown along the right side are for an average color $(V - I) = 1.5$. Eleven candidate Long Period Variables (LPVs) detected from the two separate epochs of the V -band exposures are marked with large triangles (see Section 3 of the text).

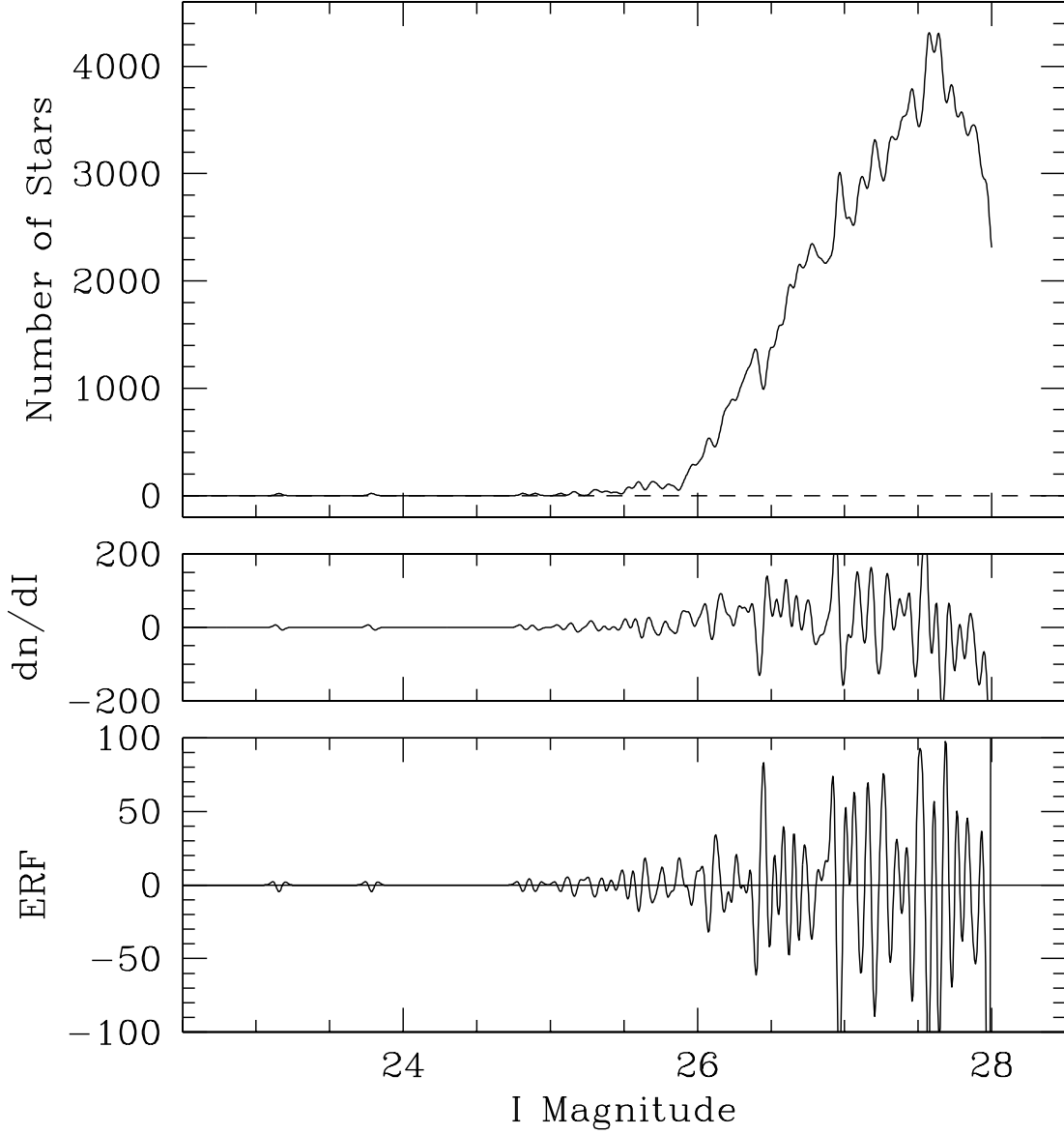


Fig. 4.— Luminosity function in I for all measured stars in the NGC 3379 field. In the uppermost graph, the number of stars per unit magnitude is plotted against I ; the middle panel shows the numerically calculated first derivative dn/dI of the LF, while the lower panel shows the numerical estimate for the second derivative d^2n/dI^2 . In all panels the data have been convolved with a Gaussian smoothing kernel of $\sigma = 0.02$ mag.

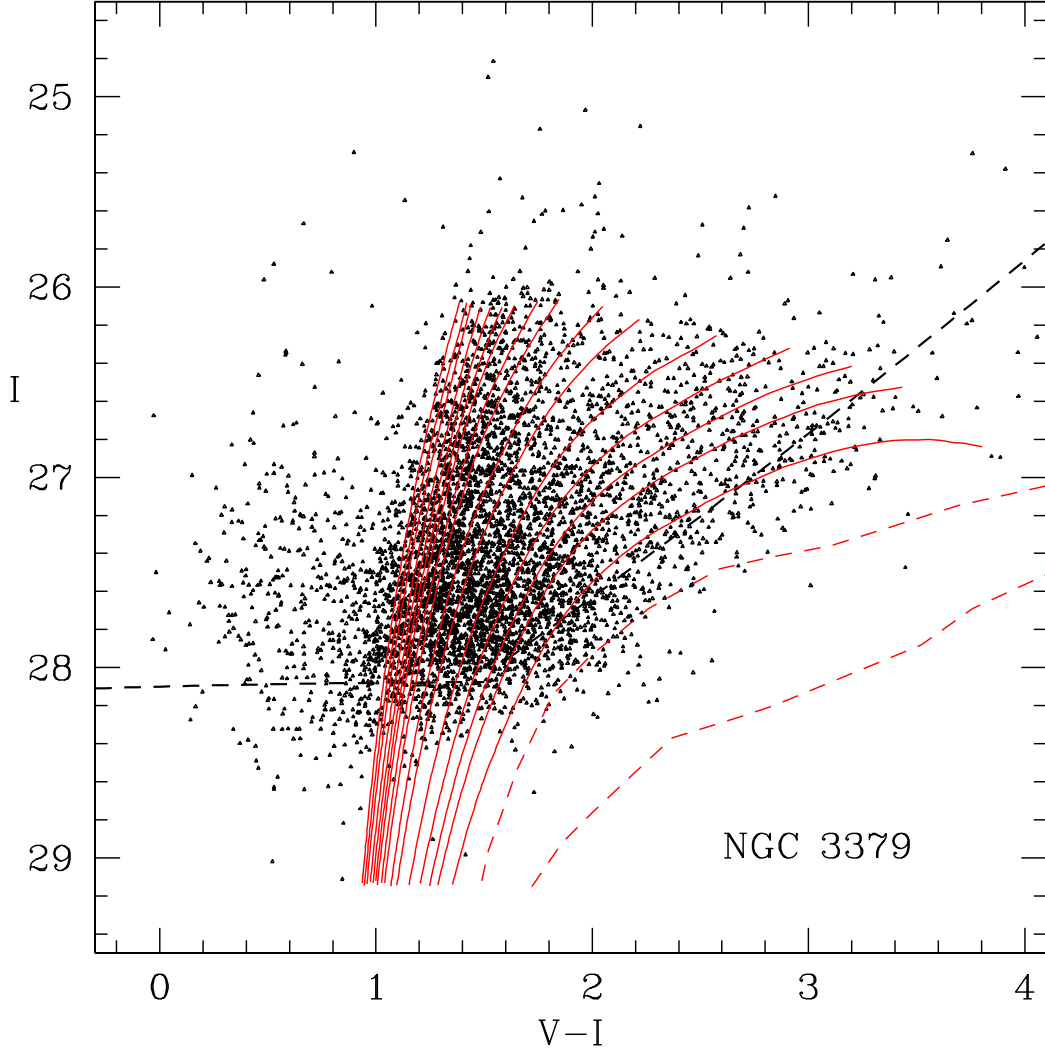


Fig. 5.— Color-magnitude diagram for the NGC 3379 red giants, with model red-giant tracks superimposed on the data points. All tracks are for ages of 12 Gyr, but differ in metallicity roughly in steps of $\Delta[\text{Fe}/\text{H}] \simeq 0.1$. These are the same set of tracks from VandenBerg et al. (2000) we have used for our previous studies of the NGC 5128 and NGC 3377 halos, supplemented by two metal-rich tracks generated from old Milky Way star clusters (see Harris & Harris 2002). The total metallicity range for the entire grid extends from $\log(Z/Z_{\odot}) = -2.0$ to $+0.4$. The placement of the tracks assumes a foreground reddening $E(V - I) = 0.02$ and a distance modulus $(m - M)_I = 30.15$ as derived in this study. The 50% photometric completeness limit is shown as the pair of dashed lines.

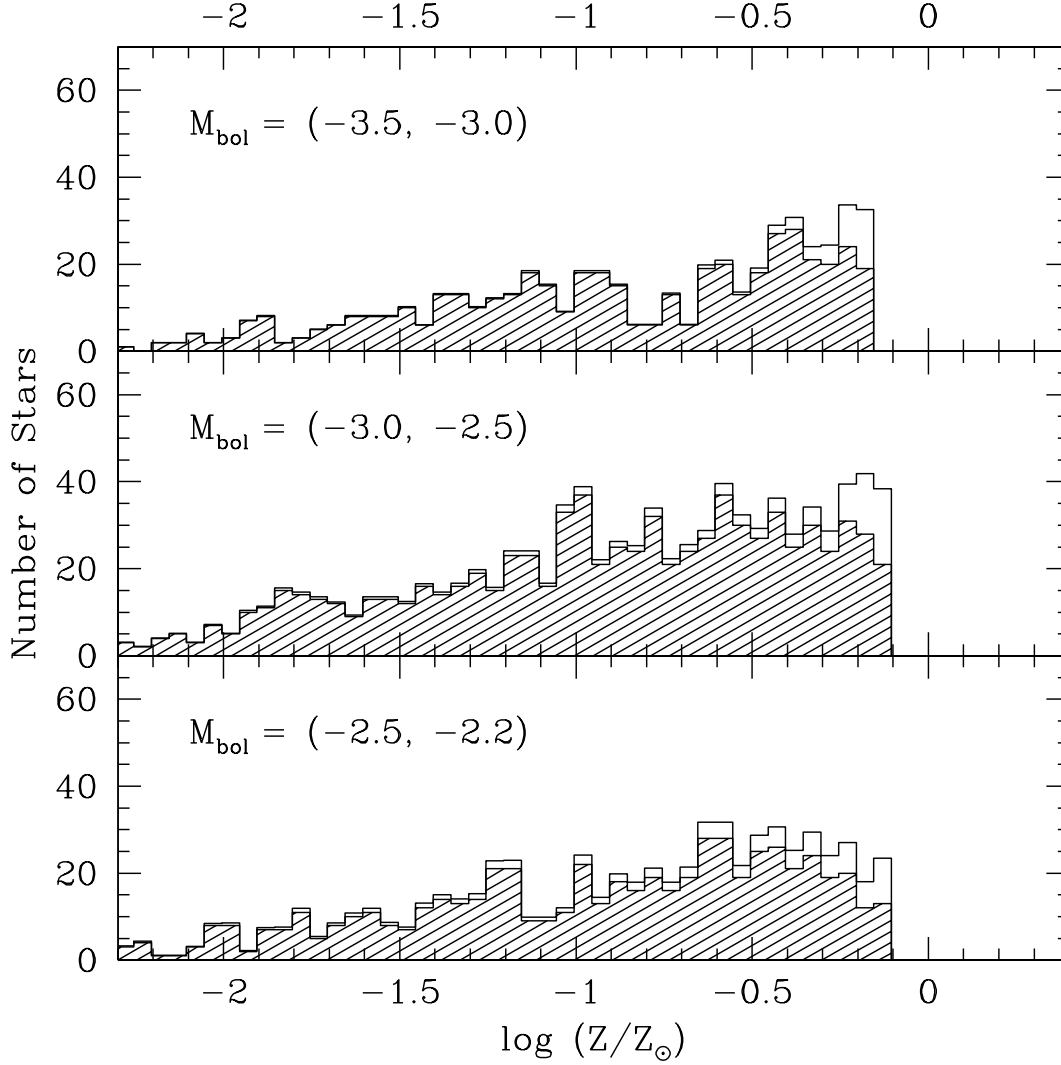


Fig. 6.— Metallicity distribution function for the halo red giants, divided into three approximate luminosity bins. This division tests for any systematic errors in the interpolation routine or the placement of the evolutionary tracks. The *shaded regions* show the MDF uncorrected for photometric completeness, while the higher *unshaded regions* show the full completeness-corrected MDF. Stars fainter than the 50% photometric completeness lines (see previous Figure) are not included in the sample, which sets the abrupt high-metallicity cutoff to the observed MDF.

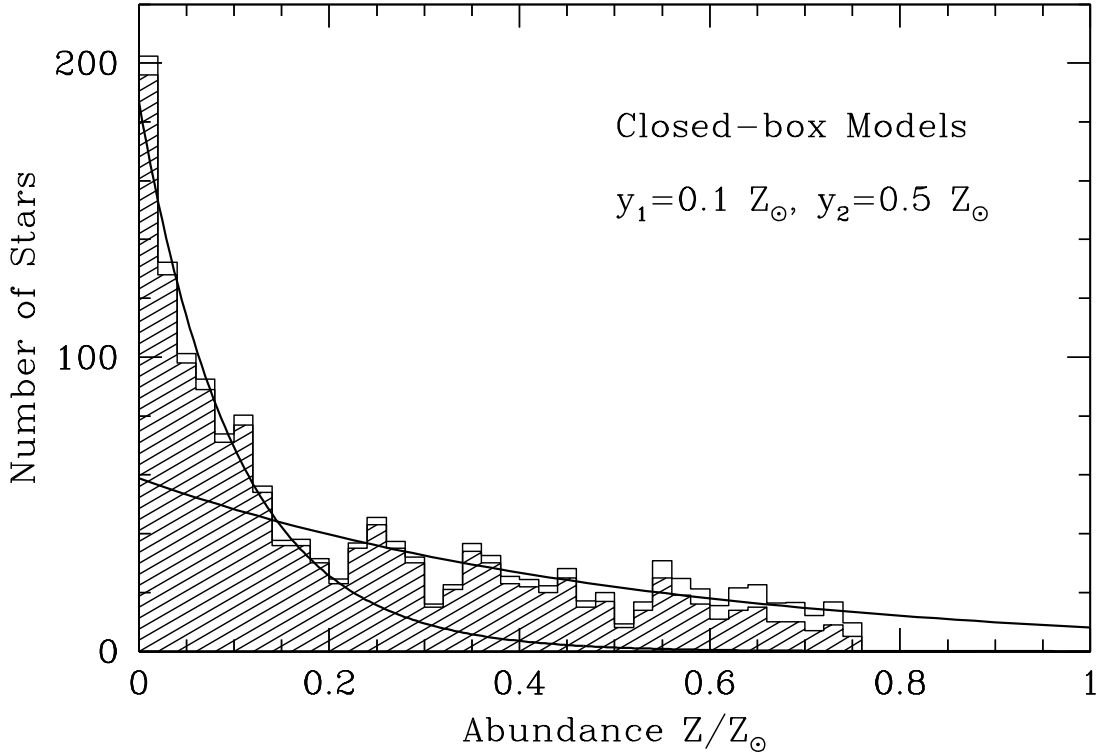


Fig. 7.— Histogram of heavy-element abundance distribution, plotted in linear form as number of stars per unit Z/Z_{\odot} . Stars from only the brightest two bins in the previous diagram ($M_{bol} < -2.5$) are used here. The predicted $N(Z)$ distributions for two separate closed-box models are shown as the solid lines. The steeper one has effective yield $y_{eff} = 0.1Z_{\odot}$, and the shallower one has $y_{eff} = 0.5Z_{\odot}$. Each one is a simple exponential decay curve with e -folding scale given by the effective yield.

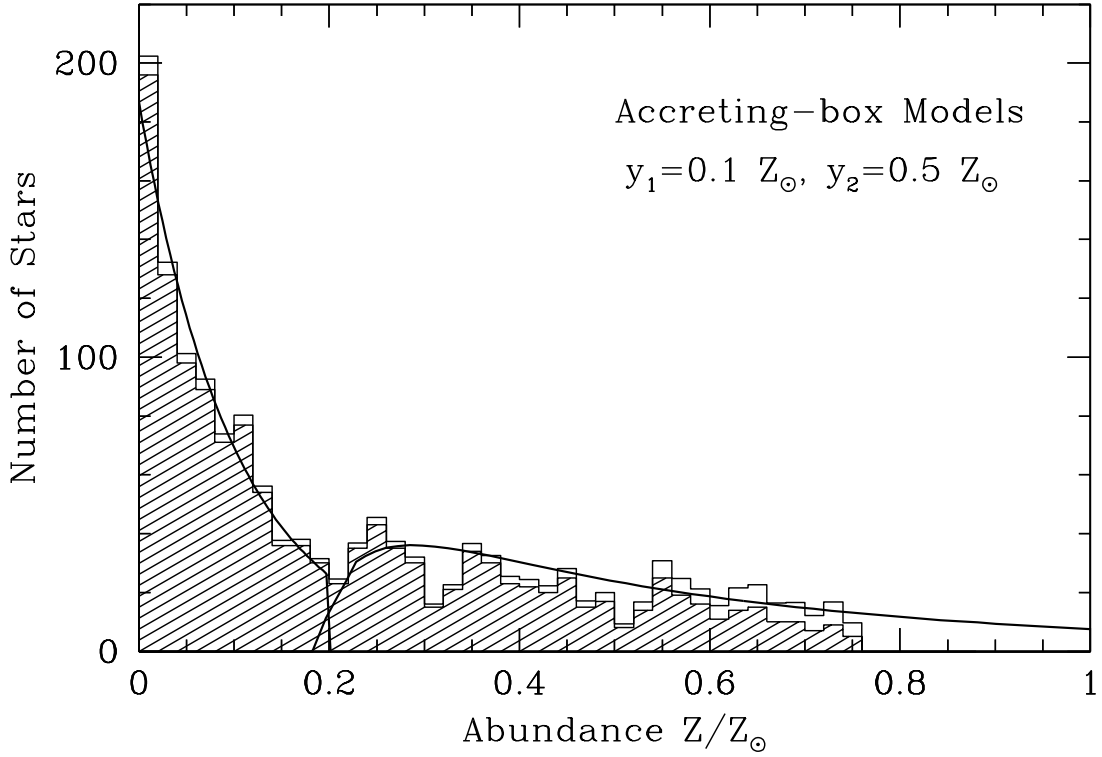


Fig. 8.— The same abundance distribution as in the previous figure, but now matched with a two-stage chemical evolution model as described in the text. The same effective yields are used as in the previous figure, but with different assumptions about the gas infall rate and abundance. The low-metallicity component ($Z < 0.2Z_\odot$) has an effective yield $y_{eff} = 0.1Z_\odot$, while the high-metallicity component ($Z > 0.2Z_\odot$) starts with pre-enriched gas and has an effective yield 5 times higher.

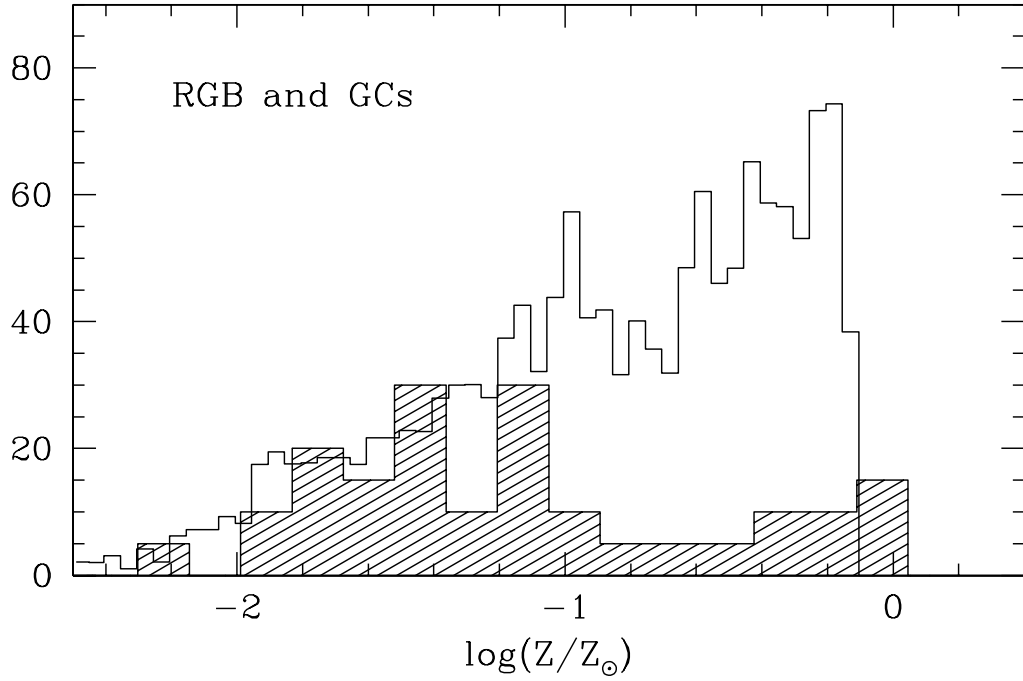


Fig. 9.— Metallicity distribution for the bright RGB stars, including the same data as in the previous graph, now compared with the metallicities of the globular clusters in NGC 3379 (data from Rhode & Zepf 2004). The RGB stars are shown as the open histogram and the GCs as the shaded histogram. For clarity we have multiplied the numbers of GCs per bin by a factor of 4 to normalize the metal-poor numbers to the RGB stars.

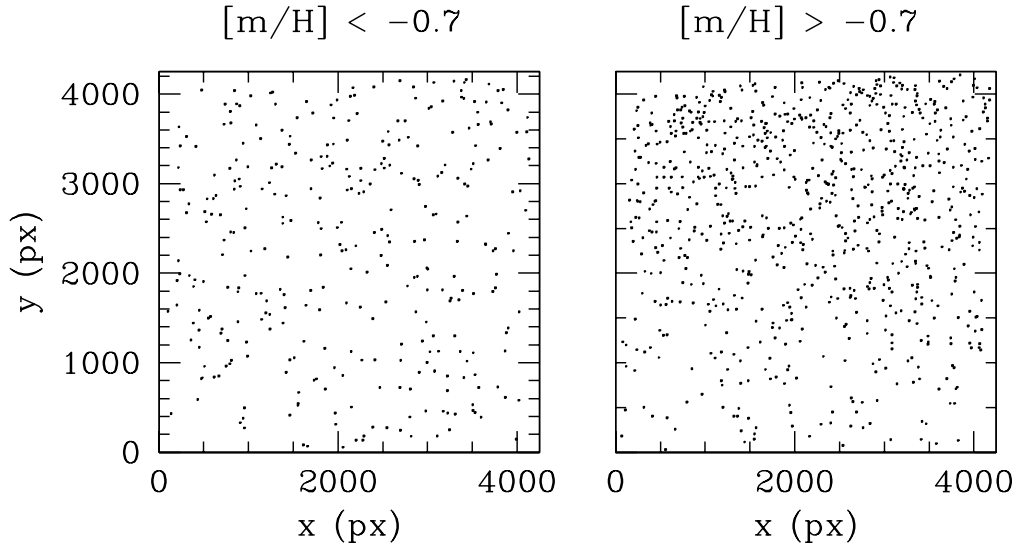


Fig. 10.— Positions of the bright stars on the ACS image, in the magnitude range $26.0 < I < 27.3$. The center of NGC 3379 is off the diagram at the top. The left panel shows the blue, metal-poor RGB stars ($[m/H] < -0.7$, equivalent to $Z < 0.2Z_{\odot}$) while the right panel shows the red, metal-rich giants ($[m/H] > -0.7$). The red population exhibits a much stronger gradient in number density across the frame.

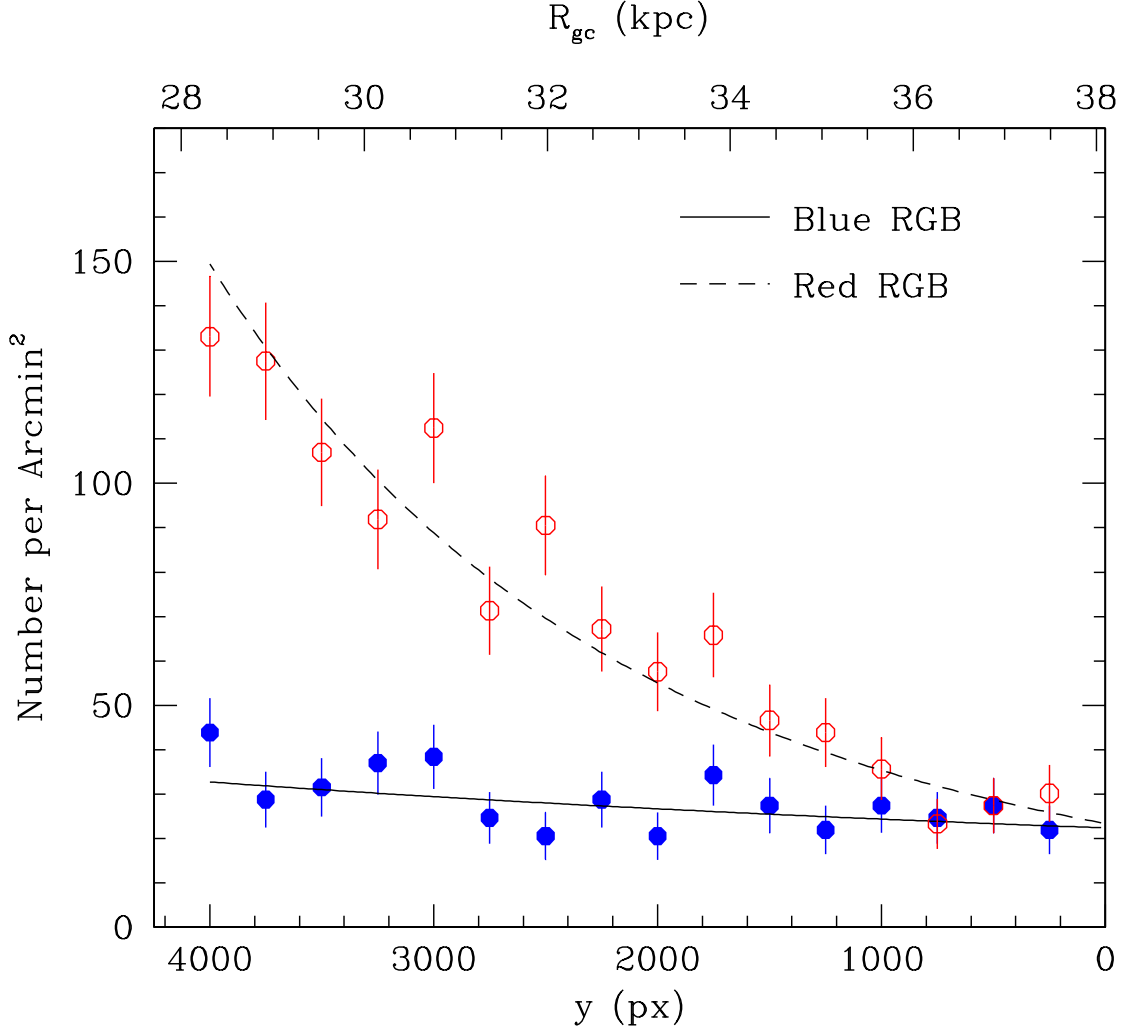


Fig. 11.— Number density σ (number of stars per arcmin²) as a function of position on the image. The solid symbols and solid line show the data for the blue, metal-poor stars with $[m/H] < -0.7$ plotted in the previous figure. The open symbols and dashed line show the same data for the red, metal-rich group with $[m/H] > -0.7$. The numbers along the top border of the plot give the projected distance R_{gc} (in kpc) from the center of NGC 3379. The blue population density falls off with radius as $\sigma \sim R^{-1.2}$ (solid curve) while the red population falls off as $\sigma \sim R^{-6.0}$ (dashed curve).

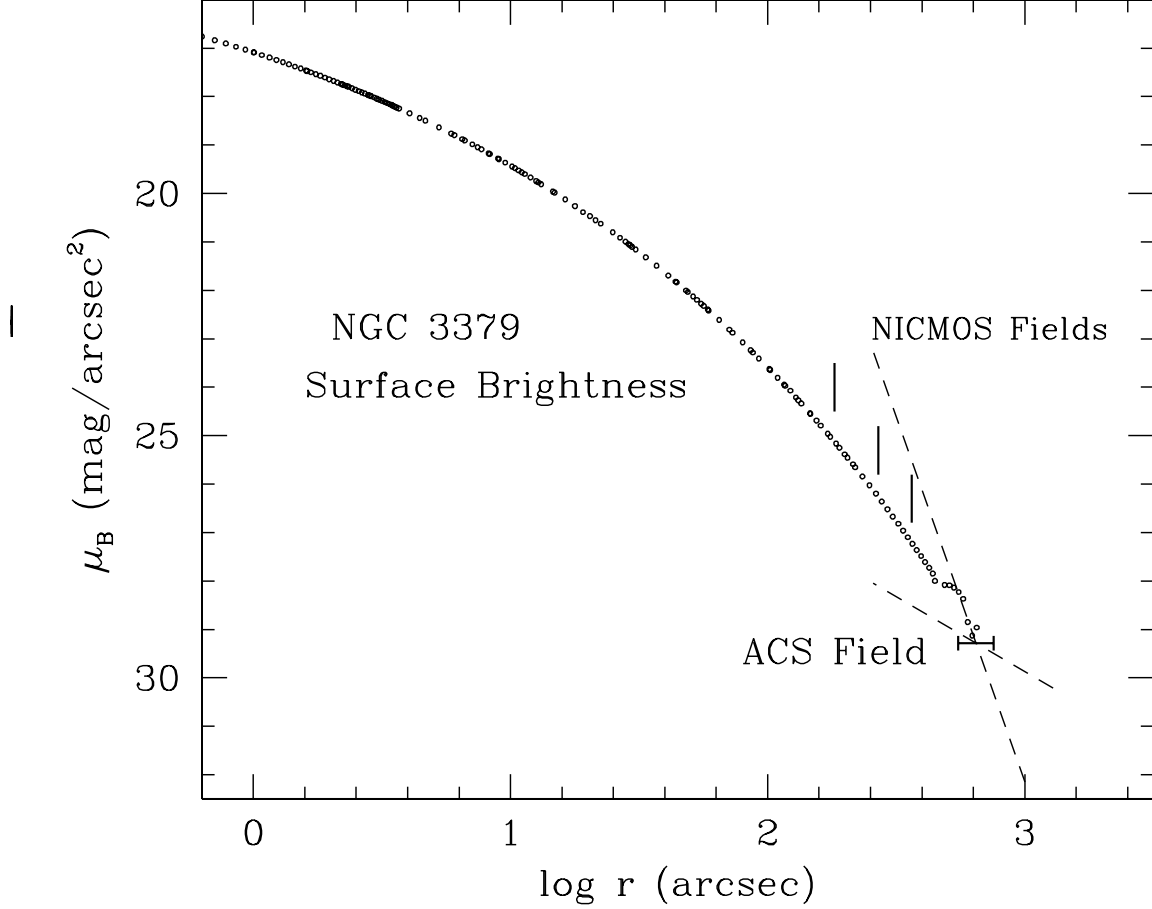


Fig. 12.— Surface brightness in B along the EW axis for NGC 3377, with data from de Vaucouleurs & Capaccioli (1979) and Capaccioli et al. (1990). The B -band surface brightness in magnitudes per square arcsecond is plotted against projected radius in arcseconds. The surface brightness measurements are shown as the dots, while the location of our ACS field is shown by the small horizontal bar at lower right (the length of the bar shows the radial extent of the field). The three vertical tick marks show the locations of the NICMOS fields studied by Gregg et al. (2004). The steeper dashed line drawn through the ACS field has a power-law exponent of -6.0 , showing the falloff rate of the redder, more metal-rich RGB stars in the previous diagram. The shallower dashed line has an exponent of -1.2 , representing the bluer, metal-poor RGB stars.

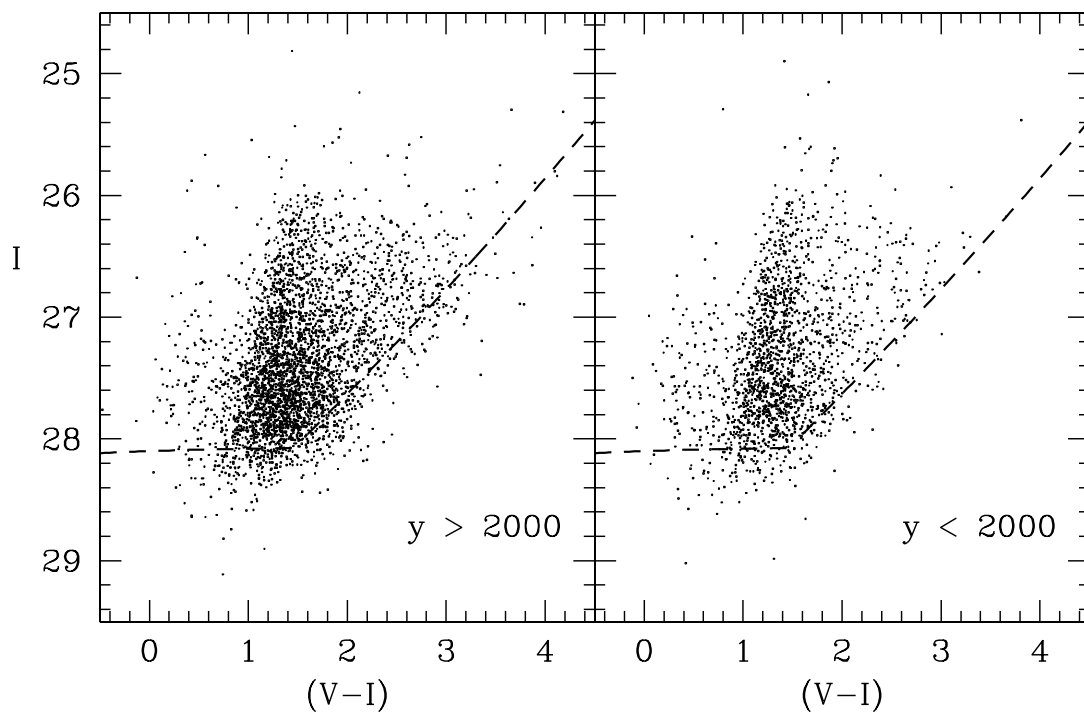


Fig. 13.— Color-magnitude diagrams for the upper (eastern) half of the frame ($y > 2000$ px) and the lower (western) half ($y < 2000$ px). The eastern half is the one closer to NGC 3379 and it has the higher proportion of red, metal-rich stars.

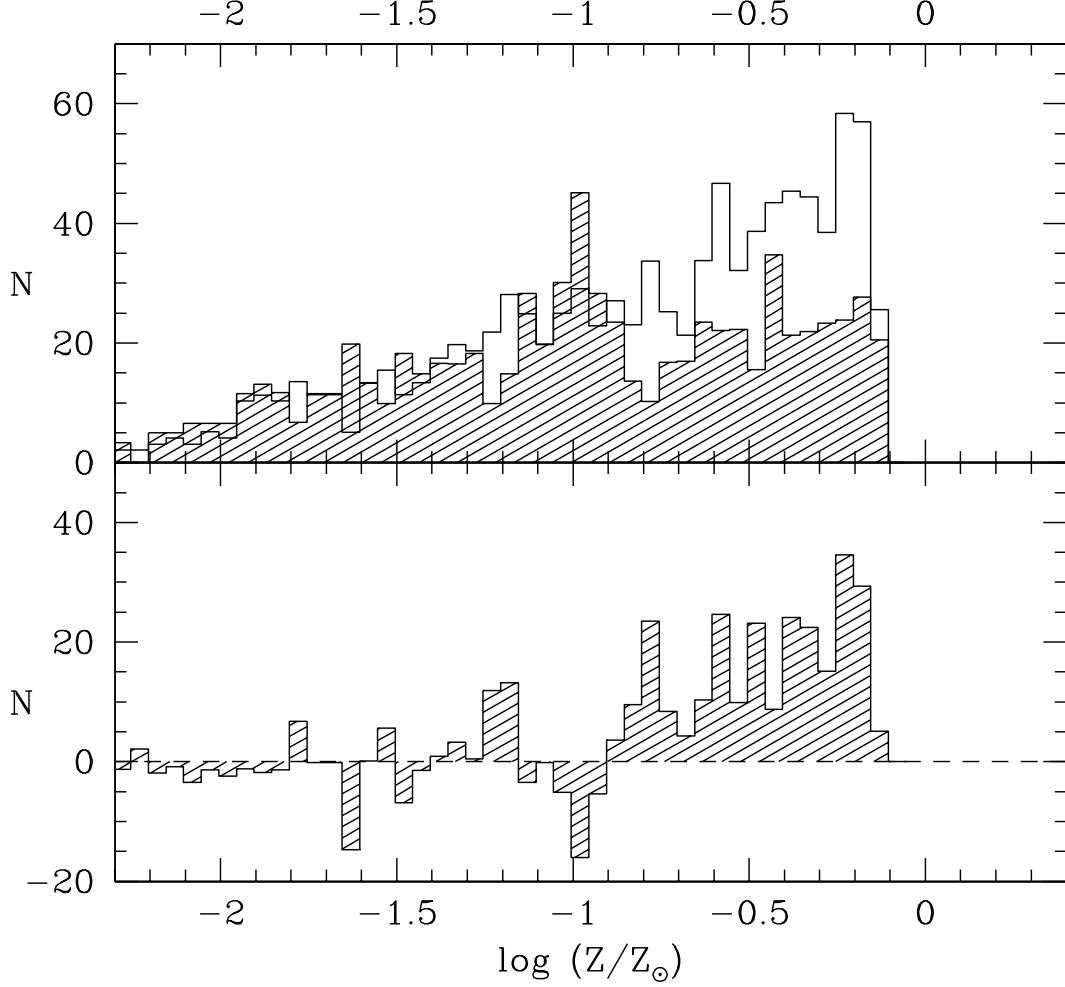


Fig. 14.— *Top panel:* Metallicity distribution for the stars in the upper half of the image ($y > 2000$ px, shown as the open histogram) and the lower half ($y < 2000$ px, shown as the shaded histogram). Both graphs have been normalized to the same total number of stars with $[m/H] < -1$. *Bottom panel:* Residual plot of the difference between the two histograms in the top panel. The upper half of the image has an excess of metal-rich stars ($[m/H] > -0.8$) relative to the metal-poor ones.

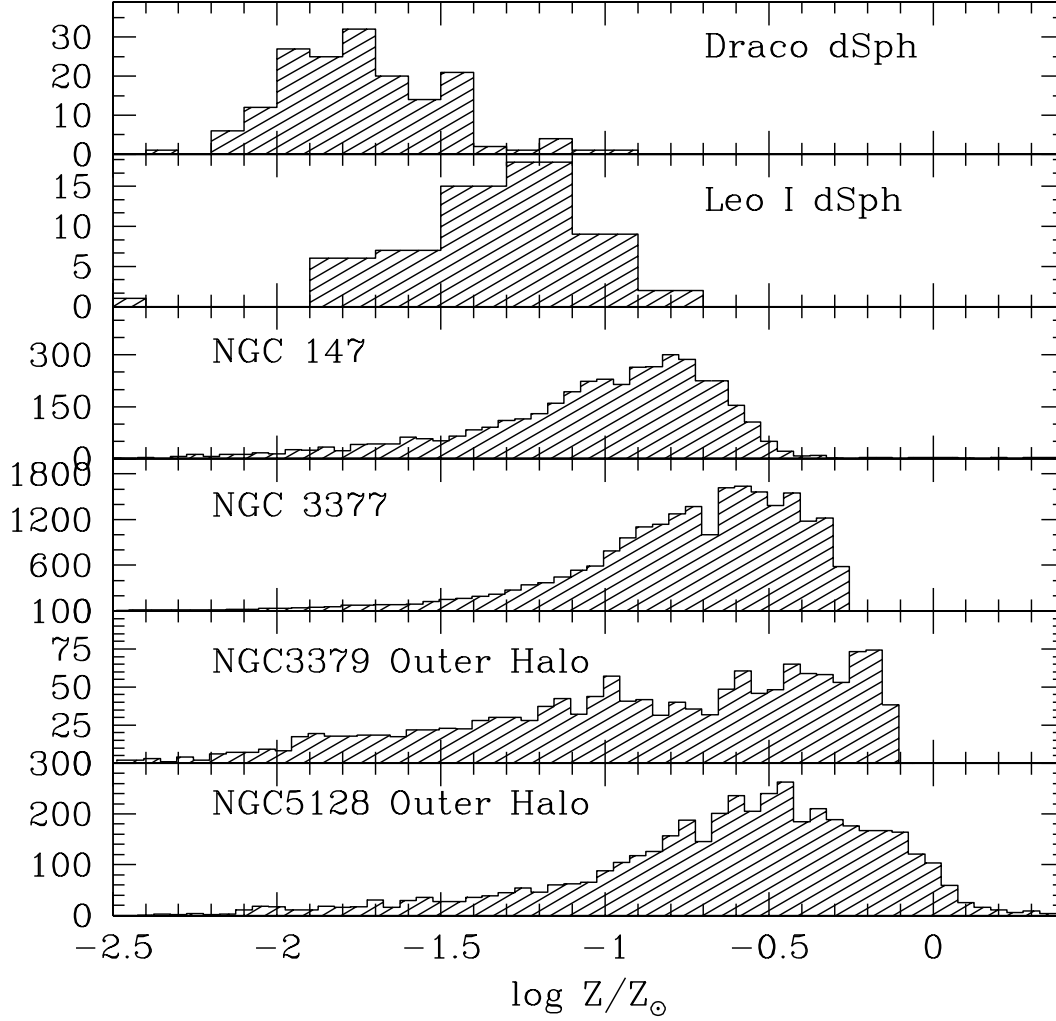


Fig. 15.— Metallicity distribution functions for 6 elliptical galaxies, including the Local Group dwarf spheroidals Draco and Leo I, the dwarf elliptical NGC 147, the Leo intermediate-luminosity elliptical NGC 3377, and the giants NGC 3379 and NGC 5128. For NGC 3377 the field shown is centered at galactocentric radius $\sim 4R_e$; for NGC 3379, $\sim 12R_e$; and for NGC 5128, $\sim 7R_e$. See text for discussion.